

TOPICAL REVIEW

High-resolution inner-shell spectroscopies of free atoms and molecules using soft-x-ray beamlines at the third-generation synchrotron radiation sources

To cite this article: Kiyoshi Ueda 2003 *J. Phys. B: At. Mol. Opt. Phys.* **36** R1

View the [article online](#) for updates and enhancements.

Related content

- [Molecular photodissociation studied by VUV and soft x-ray radiation](#)
Kiyoshi Ueda and John H D Eland
- [Symmetry-resolved soft x-ray absorption spectroscopy: its application to simple molecules](#)
Jun-ichi Adachi, Nobuhiro Kosugi and Akira Yagishita
- [Control of nuclear motion in the B 2b₂ ionic state of water via an Auger resonant Raman process](#)
A De Fanis, K Nobusada, I Hjelte et al.

Recent citations

- [Carbon and Nitrogen K-Edge NEXAFS Spectra of Indole, 2,3-Dihydro-7-azaindole, and 3-Formylindole](#)
Aurora Ponzi *et al*
- [Electron Wave Packet Interference in Atomic Inner-Shell Excitation](#)
T. Kaneyasu *et al*
- [Vibrationally resolved coupled-cluster x-ray absorption spectra from vibrational configuration interaction anharmonic calculations](#)
Torsha Moitra *et al*



IOP | ebooks™

Bringing together innovative digital publishing with leading authors from the global scientific community.

Start exploring the collection—download the first chapter of every title for free.

TOPICAL REVIEW

High-resolution inner-shell spectroscopies of free atoms and molecules using soft-x-ray beamlines at the third-generation synchrotron radiation sources

Kiyoshi UedaInstitute of Multidisciplinary Research for Advanced Materials, Tohoku University,
Sendai 980-8577, JapanE-mail: ueda@tagen.tohoku.ac.jp

Received 5 April 2002, in final form 2 December 2002

Published 12 February 2003

Online at stacks.iop.org/JPhysB/36/R1**Abstract**

This article reviews the current status of inner-shell spectroscopies of free atoms and molecules using high-resolution soft-x-ray monochromators installed in the soft-x-ray beamlines at the third-generation synchrotron radiation facilities. Beamlines and endstations devoted to atomic and molecular inner-shell spectroscopies and various types of experimental techniques, such as ion yield spectroscopy, resonant photoemission spectroscopy and multiple-coincidence momentum imaging, are described. Experimental results for K-shell excitation of Ne, O K-shell excitation of H₂O and CO₂, C K-shell excitation and ionization of CO₂ and B K-shell excitation of BF₃, obtained at beamline 27SU of SPring-8 in Japan, are discussed as examples of atomic and molecular inner-shell spectroscopies using the third-generation synchrotron radiation sources.

Contents

1. Introduction	2
2. Beamlines and endstations	4
2.1. Beamlines devoted to atomic and molecular science	4
2.2. Beamline 27SU and endstations at SPring-8	5
3. Total and partial ion yield spectroscopy	7
3.1. Ne 1s total ion yield spectrum	8
3.2. O 1s total and partial ion yield spectra of H ₂ O	9
4. Angle-resolved ion yield spectroscopy	13
4.1. Symmetries of O 1s to Rydberg transitions in H ₂ O	14
4.2. Symmetry-resolved O 1s to Rydberg excitation spectra of CO ₂	17
4.3. Symmetry-resolved C 1s \rightarrow 2 π_u excitation spectra of CO ₂	20

5. Resonant photoemission spectroscopy	23
5.1. Interference effects in resonant photoemission of Ne	24
5.2. Probing nuclear motion in the Auger final state in H_2O^+	27
5.3. Towards Doppler-free resonant Auger spectroscopy	30
6. Multiple-ion coincidence momentum imaging	31
6.1. Probing geometries for Renner–Teller states of CO_2	32
6.2. Probing molecular deformation of inner-shell excited BF_3	34
7. Electron–ion coincidence momentum imaging	37
7.1. Photoelectron angular distributions of CO_2 in the molecular frame	38
7.2. Symmetry-dependent multielectron excitation of CO_2	40
8. Concluding remarks	42
Acknowledgments	43
References	43

1. Introduction

Inner-shell spectroscopies of gaseous atoms and molecules benefit significantly from the developments of the third-generation synchrotron radiation (SR) sources and soft-x-ray monochromators. It is now possible to perform inner-shell excitations and ionizations with the monochromator bandwidth smaller than the natural width of the inner-shell excited states. In the case of atomic x-ray absorption spectra, the apparent widths of the lines often decrease with an increase in the resolution (see, for example, [1]), and higher Rydberg members emerge (see, for example, [2]). In the case of molecular x-ray absorption spectra, not only Rydberg series but also vibrational structures can be resolved well (see, for example, [3–5]).

Besides the conventional x-ray absorption spectroscopy, various types of ion yield spectroscopy, in which yields of total ions, mass-selected (i.e., partial) ions or angle- and energy-selected ions are measured as a function of photon energy, are performed at most of the SR facilities. Total ion yield spectroscopy provides us with information very similar to the x-ray absorption, whereas partial ion yield spectroscopy provides us with information about molecular dissociation dynamics intrinsic to the inner-shell excited vibronic states (see review articles [6, 7] and references therein). Angle-resolved ion yield spectroscopy, in which only the ions with kinetic energies larger than a few electronvolts are detected in the direction parallel and perpendicular to the electric vector \mathcal{E} of the incident light, provides us with information about the symmetry character of the molecular inner-shell excited states and furthermore about vibronic couplings in the excited states (see [8, 9] and a recent review article [10]). These ion yield spectroscopies become more powerful on the high-resolution monochromators installed in the linearly polarized soft-x-ray undulator beamlines at the third-generation SR facilities (see, for example, [11–18]).

Monochromatic soft x-rays from the undulator beamlines at the third-generation SR facilities are intense enough to observe inner-shell photoelectron spectra at very high resolution. One can measure intrinsic inner-shell hole lifetime widths [19–21] as well as vibronic structures of inner-shell ionized molecular ions [22–24]. Partial cross sections can also be measured for spin–orbit-split states of inner-shell ionized atomic ions [25], for molecular-field-split states of inner-shell ionized molecular ions [26], for nearly degenerate gerade and ungerade states of inner-shell ionized molecular ions [27, 28] etc. Non-dipole effects can also be investigated in the angular distributions of inner-shell photoelectrons at relatively low energies [29, 30]. Furthermore, it was demonstrated that combining high-resolution inner-shell photoelectron spectroscopy with normal Auger spectroscopy can gain detailed information about the Auger final states [31].

A narrow-band excitation also provides us with great benefits for resonant Auger spectroscopy, or photoemission study in the inner-shell excitation region. If the monochromator bandwidth is smaller than the natural lifetime width of the inner-shell excited state, the spectral widths of the resonant Auger lines are not determined by the natural width of the inner-shell excited state, but are determined by the convolution of the monochromator bandwidth, the bandwidth of the electron energy analyser and the Doppler width due to thermal motion of the sample gases [32–34]. This line-narrowing effect, often called the *Auger resonant Raman* effect, can be used for spectroscopic investigations for the Auger final ionic states. The activities in the field of atomic Auger resonant Raman spectroscopy at the second-generation facilities are well described in a review article [34]. Progress in this field at the third-generation facilities can be seen in, for example, [35–41]. Partial cross sections can also be extracted from the resonant photoemission spectra recorded as a function of photon energy, since the monochromatic soft x-rays at the third-generation facilities are intense enough to record the photoemission spectra even in the inter-resonance regions. Such partial cross section measurements turned out to reveal interference effects between the direct and resonant channels [42–46] as well as among the resonant channels [47, 48].

If resonant photoemission spectroscopy is applied to molecules, it becomes a powerful tool for investigating molecular potential energy surfaces of the inner-shell excited states and Auger final ionic states as well as nuclear dynamics along these potential energy surfaces. The lifetimes of the inner-shell excited states for light atoms such as B, C, N, O and F are of the order of 10^{-15} s. Within this timescale, however, nuclear motion of the molecule proceeds in the inner-shell excited state, and this nuclear motion can be reflected in the resonant photoemission spectrum. Activities in this field at the second-generation SR facilities are well described in a review article [49]. A number of papers on molecular resonant photoemission study have already been published using the third-generation SR facilities and probing potential energy surfaces and nuclear dynamics (see, for example, [50–71]).

Various types of coincidence experiment are also performed using monochromatic soft x-rays, in order to investigate inner-shell processes of atoms and molecules. Photoelectron–Auger-electron and Auger-electron–Auger-electron coincidences (see, for example, [72–78]), as well as Auger-electron–photoion coincidence (see, for example, [79–81]), have been carried out at various second-generation SR facilities, in order to gain insights into the atomic Auger decay processes. Such investigations are also in progress at the third-generation facilities (see, for example, [82–84]).

There are two major directions for the use of coincidence techniques in investigating molecular inner-shell processes. The first direction is the investigation of molecular fragmentation after inner-shell excitation and ionization. Molecular dissociation starts along the potential energy surface of the inner-shell excited or ionized state before the Auger decay and finishes along the potential energy surface of the Auger final state. Because of the specific shape of the potential energy surface of the inner-shell excited or ionized state, a specific dissociation channel, such as site-specific fragmentation [85], may be opened by the inner-shell excitation. Molecular fragmentation dynamics following inner-shell excitation and ionization have been investigated by means of various coincidence techniques, such as coincidence between photoelectrons or resonant/normal Auger electrons and fragment ions, coincidence among many fragment ions etc (see, for example, [86–90] and a review article [7]). The influence of the nuclear motion in the inner-shell excited states on the dissociation process can also be probed [91, 92]. Such molecular dissociation studies using coincidence techniques are also in progress at the third-generation SR facilities (see, for example, [70, 71, 93–95]).

The second direction is the measurements for angular distributions of inner-shell photoelectrons in the molecular frame (see, for example, [96–99]). This can be done by

registering the photoelectrons in coincidence with fragment ions as first demonstrated by Golovin *et al* [100]. This coincidence technique was recently extended to measurements for angular distribution of Auger electrons in the molecular frame [101, 102]. Such molecular-frame photoemission measurements are also in progress at the third-generation SR facilities (see, for example, [103–108]).

The aim of this article is to review the current status of inner-shell spectroscopies of atoms and molecules at the third-generation SR facilities. The related subjects are, however, widely spread as briefly seen above, even though the works listed above are a subset of the activities, and thus it is beyond the scope of this article to review all the activities. Instead of trying to cover most of the activities, this article describes only some specific studies on limited samples, inner-shell excitations of Ne [35, 48], H₂O [15, 16, 68, 70], CO₂ [17, 18, 93, 94, 106–108] and BF₃ [70, 71], studied at beamline 27SU of SPring-8 in Japan, one of the typical third-generation soft-x-ray beamlines devoted to gas-phase science. It is hoped that this small subset of case studies reveals the current status of atomic and molecular inner-shell spectroscopies by use of monochromatic soft x-rays with a very narrow bandwidth available at the third-generation SR sources.

In the following section, a brief account of the beamlines devoted to atomic and molecular science at the third-generation SR sources is given, and then beamline 27SU at SPring-8 is described in detail as a typical example of the devoted beamlines. Section 3 describes total and partial ion yield spectroscopies, whereas section 4 describes angle-resolved ion yield spectroscopy, as a brief review of excitation spectroscopy at very high resolution. Section 5 describes resonant photoemission studies, as a brief review of the current status for de-excitation spectroscopy. Sections 6 and 7 describe multiple-ion coincidence momentum imaging and electron–ion coincidence momentum imaging, respectively. Section 8 is a concluding remark.

2. Beamlines and endstations

2.1. Beamlines devoted to atomic and molecular science

There are several beamlines devoted to inner-shell spectroscopies of atoms and molecules at the third-generation SR sources. Such beamlines are briefly described in this subsection.

Beamline 10.0.1 at the Advanced Light Source in the US is shared by two subjects, photoemission of highly correlated materials and high-resolution atomic, molecular and optical physics, and two of the three branchlines are devoted to the latter subject. The first branchline serves the high-resolution atomic and molecular electron spectrometer endstation, the heart of which is a Scienta SES-200 electron energy analyser [109]. A series of electron spectroscopy studies have been carried out using this endstation (see, for example, [19, 20, 22, 23, 25–27, 39, 50–52]). The second branchline serves the electron spin polarization endstation [109–111] and the collinear ion–photon beamline endstation [112–114].

The gas-phase beamline 6.2R at Elettra in Italy is also devoted to the study of free atoms and molecules [115, 116]. There are multi-coincidence and angle-resolved photoemission spectroscopy endstations, and some inner-shell electron spectroscopic studies have been carried out (see, for example, [37, 42, 46, 66, 82]). Photoabsorption measurements [1–5], as well as various types of ion yield measurement [12, 13], can also be performed.

The beamline I411 at MaxII in Sweden is designed for high-resolution, angle-resolved electron spectroscopy on gases, liquids and solids [117, 118]. The endstation is equipped with a rotatable SES-200 electron energy analyser and a series of atomic and molecular works has been carried out using this endstation [21, 31, 36, 38, 44, 53–65].

One of the first molecular inner-shell photoelectron spectroscopy works at BESSYII in Germany was done at beamline U49/1, using an SES-200 electron energy analyser [24, 28].

2.2. Beamline 27SU and endstations at SPring-8

Beamline 27SU at SPring-8, nicknamed the soft-x-ray photochemistry beamline [119], is mostly devoted to gas-phase inner-shell spectroscopies. Details of this beamline and endstations are described in this subsection, as a typical example of devoted beamlines.

This beamline has a figure-8 undulator as a radiation source, and provides linearly polarized light: the electric vector \mathcal{E} is horizontal for the first-order harmonic light and vertical for the 0.5th-order harmonic light [120, 121]. The lowest energy accessible with the first-order harmonic is ~ 280 eV. One can use only the 0.5th-order light below ~ 280 eV. The degree of light polarization is almost perfect on the beam axis for the 0.5th- and first-order lights and deteriorates as one goes off the axis, goes to higher harmonics and goes to higher energy. If one restricts the acceptance angle, the degree of the polarization is better than 0.98 for 0.5th- and first-order lights. If one fully opens the acceptance angle, the degree of polarization can be deteriorated to ~ 0.97 for the 0.5th-order light, to ~ 0.8 for the first-order light and even to ~ 0.4 for the 1.5th order light, at the photon energy of ~ 900 eV. These values for the degree of polarization are measured using the Ne 2s and 2p photoelectrons and agree well with the calculations. This beamline is split into three branchlines, a, b and c. The first two are for monitoring and for use of the direct beam from the undulator. A c-branch of this beamline has a high-resolution soft-x-ray monochromator and serves inner-shell spectroscopies of free atoms and molecules.

The monochromator is of Hettrick type [122]. It has three exchangeable varied line-space plane gratings and covers the photon energy region between 150 eV and 2.5 keV [123, 124]. The highest achievable resolving power is between 10 000 and 20 000, depending on energy. For example, the values of the resolving power achieved so far are ~ 14 000 in the Ne 1s excitation region at ~ 870 eV using the first grating G1, ~ 20 000 and ~ 14 000 in the N 1s and O 1s excitation regions at ~ 400 and ~ 540 eV, respectively, using the second grating G2 and ~ 14 000 and ~ 10 000 in the B 1s and C 1s excitation regions at ~ 200 and ~ 300 eV, respectively, using the third grating G3. These estimations have been established by two independent measurements in most cases. In the first approach total ion yield spectra are recorded for sample gases, of which natural lifetime widths are known for inner-shell excited states, and curve fittings are carried out assuming that the observed line profile is the convolution between the Lorentzian profile with known width and the Gaussian profile representing the monochromator bandwidth [124]. The second approach is to estimate the monochromator bandwidth from the Xe 5p photoelectron spectra recorded by the high-resolution electron energy analyser, whose bandwidth is well characterized (see below) and can be set much narrower than the monochromator bandwidth [124]. In general, the results obtained by the two different approaches are in reasonable agreement, say, within 10–20%.

Three exchangeable refocusing mirrors of different curvatures are installed in the mirror chamber placed after the exit slit of the monochromator and used to refocus the photon beam into different experimental chambers, placed at three different positions along the photon beam.

The first experimental chamber after the refocusing mirror is for general purposes and has two experimental stages, 250 mm apart from one another, along the photon beam, in the same vacuum vessel [125]. Various types of detector and spectrometer can be installed in this chamber, depending on the experiments. One of the typical experimental arrangements is illustrated in figure 1 (see [14]). Here a long (690 mm drift tube) time-of-flight (TOF) mass spectrometer is placed on the first stage, for the partial ion yield measurements [14, 16], and a pair of detectors for energetic ions is placed on the second stage, horizontally and vertically [126], for the angle-resolved measurements of energetic ions [14–18]. An effusive beam of the sample gas can be introduced simultaneously to the source point of the TOF axis,

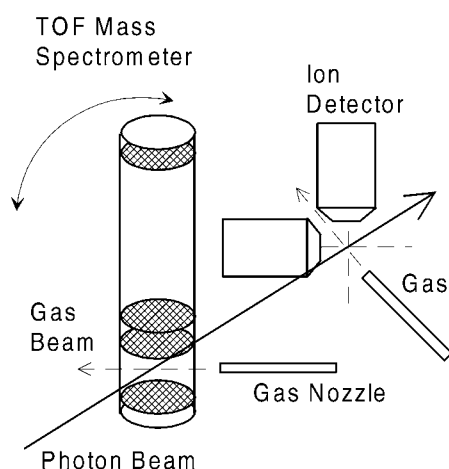


Figure 1. Schematic diagram of the experimental set-up for ion spectroscopy. The TOF mass spectrometer and the pair of energetic-ion detectors are placed in tandem along the incident photon beam, the former sitting upstream of the latter. The TOF spectrometer and its gas nozzle can be rotated from -20° to 110° with respect to the horizontal position (from [14]).

and to the crossing point of the two axes defined by the two detectors for energetic ions (see figure 1). In the TOF spectrometer, the electrons and ions are extracted with a DC electric field of $\sim 100 \text{ V mm}^{-1}$ in opposite directions: the electron signals are used to start the time-to-digital converter (TDC), while the ion signals are used to stop the TDC. In this way, the TOFs of all the fragment ions are measured simultaneously. The total ion yield can also be measured. To make this measurement, the polarity of the DC field is changed, and the ions are detected without mass selection by the electron detector of the TOF spectrometer. By use of the detectors for energetic ions, the ions with kinetic energies higher than the retarding voltage can be detected. A retarding voltage of $\sim 6 \text{ eV}$ is usually employed. The measurements are carried out for both horizontal and vertical directions, if possible, to the \mathcal{E} vector. In this way, the angle-resolved ion yield spectra compensated for the difference in the detection efficiency of the two detectors are directly obtained. A cylindrical mirror electron energy analyser can also be placed in this vessel [125, 126]. It is used for electron spectroscopy with moderate resolution (see, for example, [47, 127]) and for electron–ion coincidence experiments in combination with a short (100 mm drift length) TOF spectrometer [84].

A high-resolution electron spectroscopy apparatus is placed downstream of the general-purpose chamber and some resonant photoemission studies have been carried out (see, for example, [35, 48, 67–71]). The apparatus consists of a Gammatdata-Scienta SES-2002 hemispherical electron energy analyser, a gas cell and a differentially pumped main chamber [129]. The lens axis of the analyser is in the horizontal direction and the entrance slit of the analyser is set to be parallel to the photon beam direction. Note that one can perform the angle-resolved electron spectroscopy with the spectrometer fixed in this way, switching the direction of the electric vector \mathcal{E} from horizontal to vertical and vice versa. The whole system sits on an XYZ stage so that the source point of the analyser can be adjusted easily to the fixed photon beam position. The gas cell is operated at $\sim 10^{-3}$ Torr while the analyser vessel is maintained at $\sim 10^{-6}$ Torr. The minimum entrance slit width of the spectrometer is $200 \mu\text{m}$ and the resolving power with this slit width is ~ 1600 . The resulting minimum analyser bandwidths are $\sim 13 \text{ meV}$ for pass energy of 20 eV , $\sim 33 \text{ meV}$ for pass energy of 50 eV , $\sim 66 \text{ meV}$ for pass energy of 100 eV etc.

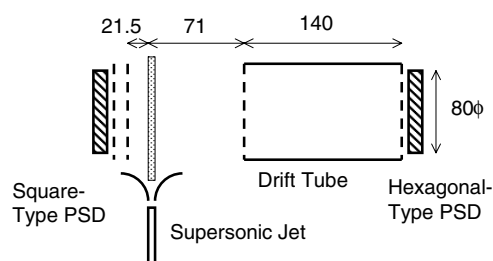


Figure 2. A schematic illustration of the multiple-coincidence momentum-imaging apparatus (from [108]).

The experimental line widths for light atoms and molecules, such as Ne and H₂O, are often dominated by the Doppler broadening due to thermal motion of the sample gases in the gas cell. Using a well collimated molecular beam instead of the gas cell, one can record electron spectra reducing the effect of the Doppler broadening significantly [128], as will be shown in section 5.3.

The high-resolution electron spectroscopy apparatus can be replaced by a multiple-coincidence momentum-imaging apparatus [70, 71, 93, 94, 106–108]. The apparatus is schematically described in figure 2. The momentum-imaging technique is based on the TOF method combined with a two-dimensional (2D) position-sensitive detector. Consider the case where one detects all the fragments in the form of atomic ions produced from the multiply charged parent molecular ions created via rapid multiple Auger decay. Registration of all the fragments allows one to extract all the kinematical information for the linear momentum (P_x , P_y , P_z) of each fragment ion, without ambiguity. A sample gas is introduced into the source volume of the imaging apparatus, in the form of a supersonic jet, and crosses the photon beam perpendicularly. The TOF axis is fixed in a horizontal direction and crosses both the light beam and the molecular beam at right angles. The ion extraction field is typically $\sim 20 \text{ V mm}^{-1}$. The length of the acceleration region is typically $\sim 70 \text{ mm}$, and the drift region is about twice as long as the acceleration region, so as to satisfy the Wiley–Maclaren space-focusing condition [130]. The TOF mass spectrometer is equipped with a multi-hit position-sensitive detector. It consists of micro-channel plates with effective diameter of 80 mm and a hexagonal-type delay-line anode (Roentdek Hex80 [131]). This recently developed three-layer delay-line anode allows us to register positions and TOFs of more than two ions with the same mass in coincidence, without suffering from the deadtime intrinsic to the conventional square delay-line anode.

Another multi-hit position-sensitive detector (Roentdek RD80 [131]) is placed on the opposite side of the TOF spectrometer, and thus the electron–ion coincidence momentum imaging can also be done using the two detectors simultaneously [106–108]. In this electron–ion coincidence mode, ions are accelerated by a uniform electrostatic field to the detector (RD80) at one end of the acceleration region, while the field accelerates electrons to the other side, where they enter the drift region. A uniform magnetic field helps drive the electrons toward the detector at the end of the drift region.

3. Total and partial ion yield spectroscopy

Dramatic progress in inner-shell absorption spectroscopy was in fact achieved at the second-generation SR sources some ten years ago with the development of high-resolution soft-x-ray monochromators (see, for example, [132–135]). A renewal of interest in inner-shell absorption

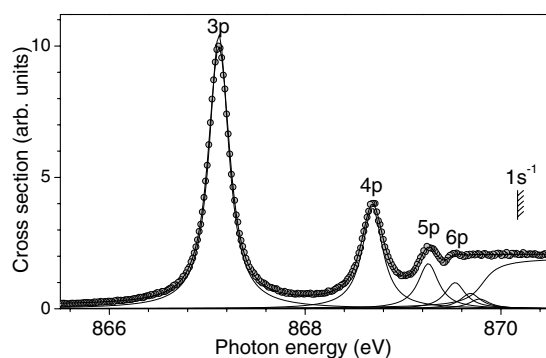


Figure 3. Circles: measured total cross section for photoionization of Ne in the $1s$ excitation region in CO_2 . Thick curve: least-squares fit, convoluted with a Gaussian with FWHM fixed to 66 meV. Thin curves: contributions from the individual resonances, before the convolution (from [48]).

spectroscopy was invoked by the unprecedented resolution achieved at the third-generation SR sources, for example at Elettra. See a series of high-resolution absorption spectroscopy studies which have been carried out at Elettra [1–5].

Measurements of total ion yields as a function of photon energy provide us with very similar information, though less quantitative, to the x-ray absorption, and are often used for performance tests of the soft-x-ray monochromators (see, for example, [118, 124]). If the monochromator resolution is very high or higher than ever achieved, total ion yield measurements can provide us with new spectroscopic information, even for well known atoms and molecules. Two such examples are presented in this section.

The first example is the Ne $1s$ absorption spectrum recorded with the photon bandwidth of 66 meV at photon energies ~ 870 eV, using total ion yield detection [48]. The Ne $1s$ absorption spectrum was previously recorded with the monochromator bandwidth of ~ 90 meV at Elettra [2] and with the monochromator bandwidth of ~ 110 meV at MaxII [118]. One finds that the $1s^{-1}6p$ resonance is partially resolved at the bandwidth of 66 meV, whereas it was not resolved in the lower-resolution measurements.

The second example is the O $1s$ absorption spectrum of H_2O recorded with the monochromator bandwidth of 55–40 meV, using total ion yield detection [16]. The O $1s$ absorption spectrum of H_2O was previously recorded with a monochromator bandwidth of ~ 120 meV [135]. One finds that the vibrational structure at the O $1s^{-1}2b_2$ resonance, which was not resolved with the bandwidth of ~ 120 meV, is resolved with the bandwidths of 55–40 meV.

If the molecular inner-shell absorption spectrum exhibits vibrational structure, partial ion yield spectroscopy is very powerful in investigating the influence of the nuclear motion in the inner-shell excited states on the molecular dissociation. A typical example can be seen in partial ion yield measurements for H_2O [16], where the branching ratio to the H_2^+ formation increases with an increase in the vibrational energy stored in the O $1s^{-1}2b_2$ inner-shell excited state.

3.1. Ne $1s$ total ion yield spectrum

The ground state neon atom has the electronic configuration $1s^2 2s^2 2p^6$. The total ion yield spectrum in the region of the $1s \rightarrow np$ Rydberg excitation is shown in figure 3, together with a least-squares fit (see below). The spectral dependence of the total ion yield is equivalent to that of the photoabsorption cross section. The monochromator bandwidth is ~ 66 meV, as

estimated from Xe 5p photoelectron spectra. The photon energy scale in figure 3 is calibrated by using the energies of the $1s^{-1}3p$ and $1s^{-1}4p$ resonances reported in [2]. This spectrum is similar to the one presented in [2], but the resolution in figure 3 is slightly higher and thus the $1s^{-1}6p$ resonance is partially resolved.

Photoabsorption cross sections in the inner-shell excitation regions are usually analysed with the following expression [136]:

$$\sigma = \sigma_{\text{dir}} + \sum_m \frac{\sigma_m}{1 + \epsilon_m^2} + \sigma_{1s}, \quad (1)$$

where m labels the resonances and $\epsilon_m = (h\nu - E_m)/(\Gamma_m/2)$ are the distances of the photon energy $h\nu$ from the resonant energies E_m measured in terms of half natural widths (HWHM) $\Gamma_m/2$. σ_m and σ_{dir} are the cross sections for resonant and direct ionization. $\Gamma_m/2$, σ_m and σ_{dir} are considered constant in the energy interval of interest. The term σ_{1s} in equation (1) represents the $1s$ ionization cross section:

$$\sigma_{1s} \propto \frac{1}{2} + \frac{1}{\pi} \arctan[2(h\nu - E_{1s})/\Gamma]. \quad (2)$$

In the fitting routine, the expression (1) is convoluted with a Gaussian profile with fixed FWHM of 66 meV in order to simulate the photon bandwidth. The fit extracts the line strengths, Lorentzian widths and energies of the resonances. Although $1s^{-1}7p$ and $1s^{-1}8p$ cannot be resolved, they are also included in the fit, in order to reach an overall better agreement between the fit and the measurement. Contributions from higher members are included in σ_{1s} . Some parameters are fixed using quantum defect methods [137]. Namely, the energies of the $1s^{-1}6p$ – $1s^{-1}8p$ resonances are fixed to the values extrapolated from the $1s^{-1}3p$ – $1s^{-1}5p$ resonances, whereas the line strengths of $1s^{-1}7p$ and $1s^{-1}8p$ relative to the line strength of $1s^{-1}6p$ are fixed. The widths are assumed to be the same for the resonances $1s^{-1}4p$ – $1s^{-1}8p$. The widths for these high- n members, however, turn out to be the same as that of $1s^{-1}3p$ via fitting within the experimental uncertainties. The value thus obtained for the natural lifetime width, $\Gamma_{3p} = 240 \pm 10$ meV, is slightly lower than the calculated one in [2], $\Gamma_{3p} = 258$ meV.

It should be noted that each Lorentzian profile included in equation (1) is the limit $q \rightarrow +\infty$, but $\sigma_a q^2$, which is related to the oscillator strength of the line, is still a certain finite value, in the resonance formula of Fano [138]:

$$\sigma = \sigma_a \frac{(q + \epsilon)^2}{1 + \epsilon^2} + \sigma_b. \quad (3)$$

Here q is the Fano profile index and σ_a and σ_b are the cross sections for excitation to the continuum that does and does not interact with the discrete isolated resonance. Although the interaction of the resonances with the continuum channels may not be negligible, as we will discuss later, the Lorentzian profiles in expression (1) are still a good approximation for the resonant profiles in the total cross section, as can be seen in figure 3.

3.2. O $1s$ total and partial ion yield spectra of H_2O

The H_2O molecule has a geometric structure that belongs to the C_{2v} point group ($r(O-H) = 0.958$ Å; $\theta_{H-O-H} = 104.4^\circ$) [139] in the ground state, and the electronic configuration is [140]

$$1a_1^2 2a_1^2 1b_2^2 3a_1^2 1b_1^2; 4a_1^0 2b_2^0 (^1A_1).$$

Here $1a_1$ and $2a_1$ are O $1s$ and O $2s$ orbitals, respectively. The outermost orbital $1b_1$ has mostly the out-of-plane O $2p_x$ character, while the in-plane components O $2p_z$ and O $2p_y$ combine with H $1s$ and form the O–H bonding orbitals $3a_1$ and $1b_2$, respectively. The unoccupied orbitals $4a_1$ and $2b_2$ are the antibonding counterparts of these two orbitals. There are three

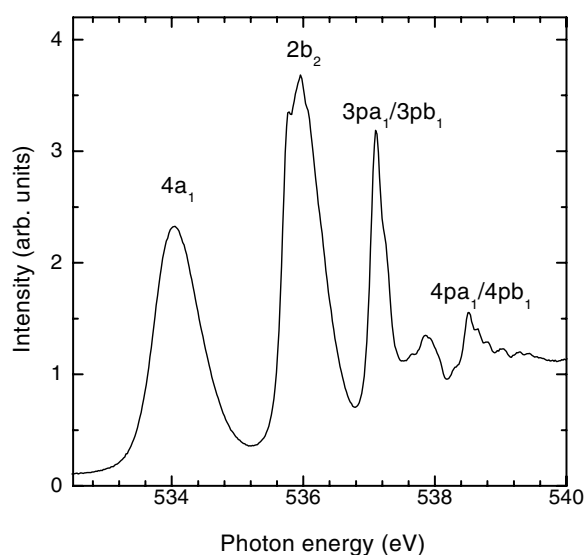


Figure 4. The total ion yield spectrum of H_2O in the O 1s excitation region (from [16]).

vibrational modes in the H_2O molecule of point group C_{2v} : the symmetric stretching mode ν_1 of a_1 symmetry, the bending mode ν_2 of a_1 symmetry and the asymmetric stretching mode ν_3 of b_2 symmetry.

Figure 4 shows the total ion yield spectrum of H_2O in the whole O 1s excitation region [16]. The monochromator bandwidth is ~ 55 meV. The broad bands at 534 eV ($4a_1$) and 536 eV ($2b_2$) correspond to the promotions of the electron from O 1s to the unoccupied molecular orbitals $4a_1$ and $2b_2$, respectively, whereas the structures between 537 and 540 eV are due to the transitions to the Rydberg members [135]. We will discuss the Rydberg structure later. The O 1s $\rightarrow 4a_1$ band shows no vibrational structure. This observation confirms the dissociative character of this state, as reported previously [135].

In contrast to $4a_1$, the $2b_2$ band exhibits vibrational structures with obvious peaks at 535.74, 535.95 and 536.08 eV and a bump at 535.85 eV, as presented in the slightly higher resolution spectrum (bandwidth ~ 40 meV) in figure 5(a). The vibrational structures become less clear on the higher-energy side of the $2b_2$ band. The observed vibrational structure cannot be explained by a simple progression of one vibrational mode. To proceed with the analysis of the vibrational structure, a least-squares peak fitting is carried out for the entire $2b_2$ band. In the peak fitting, two vibrational modes, ν_1 and ν_2 , both with constant vibrational spacings (harmonic approximation), are assumed, and each peak is assumed as a convolution of a Gaussian profile with 40 meV FWHM and a Lorentzian profile whose FWHM has the lower-limit value of 150 meV, i.e., the inner-shell hole lifetime width [142], at the first peak at 535.74 eV, and increases linearly with an increase in the vibrational energy. The energy-dependent Lorentzian width was necessary for the reasonable fitting, suggesting that higher vibrational states are dissociative. The Lorentzian width as a function of vibrational energy E_{vib} turned out to be $0.15 + 0.1E_{\text{vib}}$ (eV) via the fitting. The vibrational spacings obtained via fitting are 215 ± 5 and 114 ± 5 meV, as seen in figure 5(a). An even number of ν_2 vibrational states may not be distinguished from the ν_1 sequence, because the frequency of ν_1 is about twice the frequency of ν_2 . A similar analysis is carried out for D_2O , as shown in figure 5(b). Reasonable fitting is obtained for 151 ± 5 meV for ν_1 and 80 ± 5 meV for ν_2 , using a frequency reduction factor of 0.7 from H_2O to D_2O . The consistent fitting between H_2O and D_2O for the

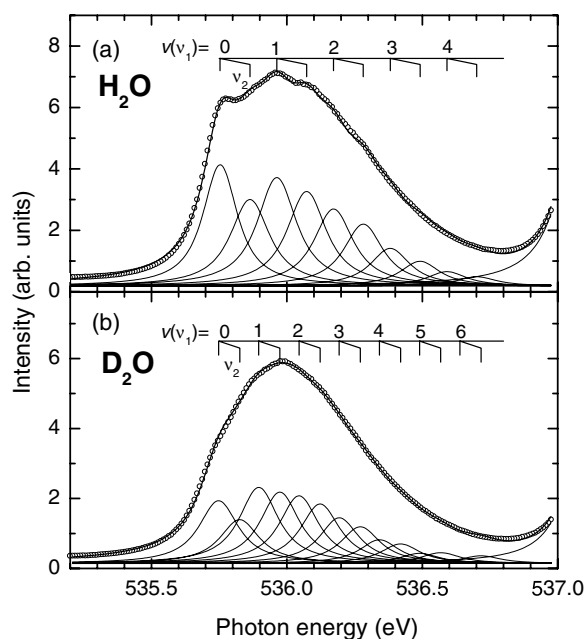


Figure 5. High-resolution (~ 40 meV) spectra of H_2O (a) and D_2O (b) in the region of the $2b_2$ band. The solid curves are the result of the least-squares peak fit (from [16]).

vibrational structures indicates the validity of the analysis and eliminates the possibility of the overlap of another electronic state in this resonance.

Two *ab initio* calculations have been carried out for the potential energy surfaces of inner-shell excited states in H_2O [16, 68]. First the calculations were carried out using the equivalent-core approximation, in which the O $1s$ excited states are approximated by the relevant states of FH_2 [16]. It was predicted that the O $1s^{-1}2b_2$ state has a C_{2v} stable geometry which is quite different from the ground state: the O–H bond is elongated by 0.25 \AA and the H–O–H angle is 10° less. Because of the change of both the bond length and the bond angle, one can expect that both symmetric stretching and bending vibrations are caused by the O $1s \rightarrow 2b_2$ excitation. The vibrational frequencies in this stable geometry in O $1s^{-1}2b_2$ are estimated to be 186 meV for the symmetric stretching vibration, ν_1 , and 124 meV for the bending vibration, ν_2 , in reasonable agreement with the experimental results. The *ab initio* potential energy surfaces based on the equivalent-core approximation were confirmed later [68] by calculations without using the equivalent-core approximation. Both *ab initio* studies indicated that the symmetric stretching and bending motions are coupled, and thus ν_1 and ν_2 have both symmetric stretching and bending character.

Piancastelli *et al* [141] observed the H_2^+ formation from H_2O^+ via the O $1s \rightarrow 2b_2$ excitation in H_2O . They suggested a key role of the bending motion in the inner-shell excited state, though they could not resolve the vibrations with their limited resolution ($\sim 180 \text{ meV}$ bandwidth) and thus could not exclude the possibility of overlap with another electronic state. In a similar measurement, with the bandwidth of $\sim 55 \text{ meV}$ [16], vibrations in the inner-shell excited state are resolved, and clear evidence is obtained for the role of the vibrations in the inner-shell excited state.

Figure 6 shows the H_2^+ ion yield curve (b) and the intensity ratio of H_2^+ (c) relative to the total ion yield given in (a), as a function of the excitation photon energy. The H_2^+ ion yield curve

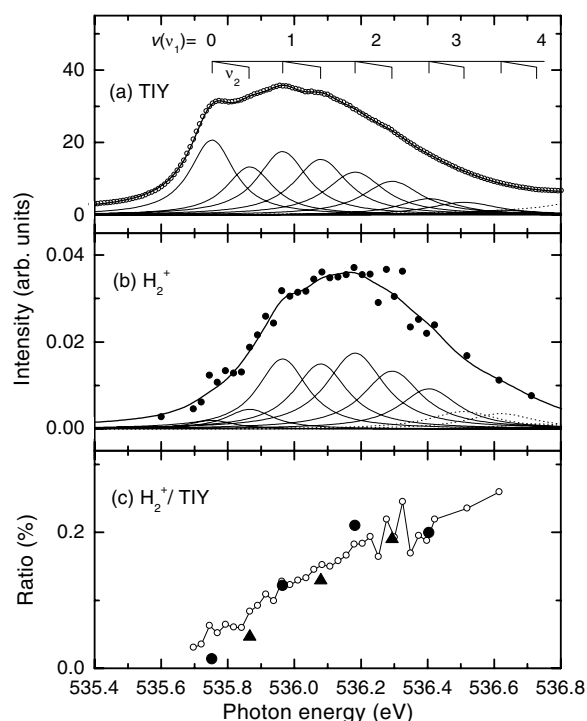


Figure 6. The total ion yield spectrum (a), the H_2^+ yield spectrum (b) and the ratio H_2^+ to the total ion (c) in the $\text{O } 1s^{-1}2b_2$ resonance. Solid line in (b), fitting to the experimental results given by full dots. The scatter of the dots indicates the experimental uncertainties. Open circles in (c), estimated from the yield curves in (a) and (b). Closed circles and triangles in (c), estimated from the area of each vibrational component in (a) and (b) obtained via least-square fit, for $(n, 0)$ and $(n, 1)$, respectively (from [16]).

is also analysed in the same way as the total ion curve, and the intensity ratio H_2^+ to the total ions for each vibrational quantum state is also plotted in figure 6(c). The reaction rate for the H_2^+ formation increases linearly with an increase in the internal energy stored in the $\text{O } 1s^{-1}2b_2$ inner-shell excited state. The linear dependence of the H_2^+ formation on the internal energy of the inner-shell excited state clearly demonstrates that the H_2^+ formation is mediated by the nuclear motion in the inner-shell excited state. The fact that H_2^+ formation is independent of vibrational modes excited, ν_1 or ν_2 , is in accordance with the theoretical prediction that the symmetric stretching and bending motions are coupled.

Ab initio calculations have been carried out for potential energy surfaces of the Auger final states, in order to find the reaction pathway to H_2^+ formation in the Auger final states. In the independent particle approximation, the resonant Auger transition is classified into two groups. If the excited electron participates in the Auger decay, the decay is called *participator Auger decay*. The final state of this decay is the same as that of the direct photoemission from the valence orbital. If the excited electron behaves as a spectator in the Auger decay, the decay is called *spectator Auger decay*. The final states of the spectator Auger decay are two-hole, one-particle in the valence orbitals. Here we focus on the spectator Auger final state $1a_1^2 2a_1^2 1b_2^2 3a_1^2 2b_2^1$ (2^2B_2) corresponding to the $\text{O } 1s \rightarrow 2b_2$ excitation. Figure 7 presents the potential energy curves of the spectator Auger final state of $\text{H}_2\text{O}^+(2^2B_2)$ as a function of the H–O–H angle [16]. Both of the O–H internuclear distances, r , are fixed at some representative values. The figure clearly shows that H_2O^+ becomes much more stable energetically with an

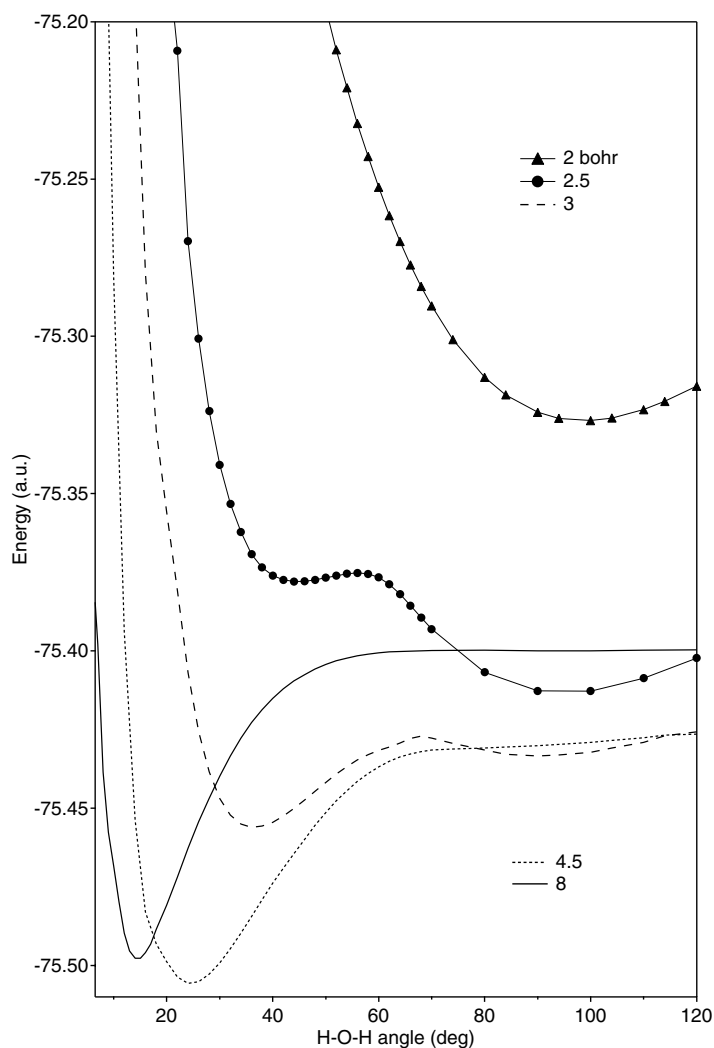


Figure 7. Potential energy curves of the spectator Auger final state ($1a_1^2 2a_1^2 1b_2^2 3a_1^2 2b_2^1; 2^2 B_2$) as a function of the H–O–H angle. The calculations are carried out keeping the C_{2v} point group. The O–H distances are fixed at 2, 2.5, 3, 4.5 and 8 bohr (from [16]).

increase in the O–H distance and a decrease in the H–O–H angle. At $r \geq 4.5$ bohr, the potential curve has a deep well. At sufficiently larger r the potential curve almost coincides with the diatomic H_2^+ potential. In fact, the depth of the potential well at $r = 8$ bohr is approximately equal to the dissociation energy of H_2^+ ($=2.65$ eV). From these characteristic features of the potential energy curves, one can expect that H_2O^+ dissociates into $O + H_2^+$ and that this H_2^+ formation channel is promoted by making the H–O–H angle smaller and the O–H distance larger before the Auger decay. These theoretical analyses are in good agreement with the experimental observations described above.

4. Angle-resolved ion yield spectroscopy

The angular distribution of fragment ions provides information about symmetries of inner-shell excited states in linear molecules [143–145]. One often calls the measurement of the

ion yield spectra, $I(0^\circ)$ and $I(90^\circ)$, of linear molecules, detected in the directions parallel and perpendicular to the electric vector \mathcal{E} , *symmetry-resolved absorption spectroscopy* [8, 9], because $I(0^\circ)$ and $I(90^\circ)$ dominantly reflect the $\Sigma \rightarrow \Sigma$ and $\Sigma \rightarrow \Pi$ transitions, respectively, for linear molecules. This symmetry resolution relies on the fact that the inner-shell hole decay and dissociation rates are much faster than the molecular rotation, and thus the axial-recoil approximation [146–148] is valid. The applications of this technique to polyatomic molecules of different point groups, such as C_{2v} [149] and D_{3h} [88], are straightforward.

In this section we will first discuss the O 1s to Rydberg excitations of H_2O observed in the angle-resolved ion yield spectra [15]. In contrast to the O 1s $\rightarrow 2b_2$ excitation discussed in section 3.2, the O 1s \rightarrow Rydberg excitation includes many electronic states, with three different symmetries, A_1 , B_1 and B_2 , and one finds difficulty in assigning the peak structures observed in the total ion yield spectrum. Angle-resolved ion yield spectroscopy is very powerful in the assignments of the observed structures in such a situation.

The second example presented here is the O 1s to Rydberg excitations of CO_2 observed in the angle-resolved ion yield spectra [18]. Symmetry breaking of the inner-shell excited states can be generalized as a result of vibronic coupling via non-totally symmetric nuclear motion [150–153]. The excitation of the O 1s inner-shell electron, for example, leads to symmetry-lowering as a consequence of vibronic coupling, referred to as pseudo-Jahn–Teller coupling [150, 151], which mixes the nearly degenerate inner-shell excited states, O 1s $1\sigma_g^{-1} nl$ and O 1s $1\sigma_u^{-1} nl$, via the antisymmetric stretching vibration ν_3 . The inner-shell excited state then becomes unstable along the antisymmetric stretching coordinate Q_3 . As a result, the antisymmetric stretching motion ν_3 is caused in the inner-shell excited state. The symmetry breaking and the excitation of the antisymmetric stretching mode have been discussed extensively in the analysis of the O 1s photoelectron spectra [150, 154, 155] and the O 1s resonant soft x-ray emission spectra [156–158]. The effect of this pseudo-Jahn–Teller coupling can also be probed in the high-resolution symmetry-resolved O 1s to Rydberg excitation spectra [18].

The last example is the C 1s $\rightarrow 2\pi_u$ excitation spectra of CO_2 [17]. The excitation of the C 1s inner-shell electron to $2\pi_u$ leads to the doubly degenerate Π_u state that splits into two states along the bending coordinate Q_2 , referred to as the static Renner–Teller (RT) effect [51, 159–161]. As seen in figure 8, the lower branch of the RT states has a stable bent geometry. This bent state has an electron in the π_u orbital that lies in the bending plane of the molecule (in plane, A_1 in C_{2v}). The upper branch, on the other hand, remains linear. This linear state has an electron in the π_u orbital that lies perpendicular to the bending plane (out of plane, B_1 in C_{2v}). Symmetry-resolved excitation spectra for the C 1s $\rightarrow 2\pi_u$ A_1 and B_1 resonances will be presented and discussed [17].

4.1. Symmetries of O 1s to Rydberg transitions in H_2O

Figure 9 shows the ion yield spectra of H_2O and D_2O in the region of O 1s to Rydberg excitation [15]. Panels (a) and (d) are the yield spectra $I(0^\circ)$ and $I(90^\circ)$ of the energetic ions (≥ 6 eV), recorded in the 0° and 90° directions with respect to the \mathcal{E} vector, for H_2O and D_2O , respectively. Here the energetic ions are H^+ produced via dissociation from the dissociative spectator Auger final states. The total ion yield spectra for H_2O and D_2O are also given in panels (b) and (e), respectively. The anisotropy parameter β for energetic ions is obtained from the measured quantities $I(0^\circ)$ and $I(90^\circ)$ by use of the relation

$$\beta = \frac{2[I(0^\circ) - I(90^\circ)]}{I(0^\circ) + 2I(90^\circ)}. \quad (4)$$

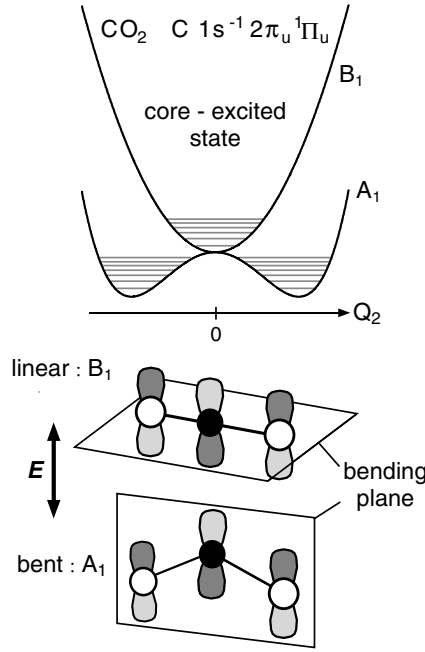


Figure 8. A schematic representation of the Renner–Teller states split from $C\ 1s^{-1}2\pi_u^1\Pi_u$. The geometries of the $2\pi_u$ orbital and the bending planes of the A_1 and B_1 states are shown in the lower part (from [93]).

The values of β thus obtained for H_2O and D_2O are plotted in panels (c) and (f), respectively. The quantity $I(0^\circ) + 2 \times I(90^\circ)$ and total ion yield are roughly proportional to the photoabsorption but are not exactly the same, since the total ion measurements are more sensitive to the double-ionization events than the single-ionization events, whereas the energetic-ion measurements detect only the events which produce ions with kinetic energy ≥ 6 eV. Angle-resolved ion yield spectra were recorded previously at the monochromator bandwidth ~ 700 meV [149]. The spectra in figure 9 recorded at the monochromator bandwidth ~ 40 meV exhibit much more Rydberg and vibrational structure.

The dipole-allowed transitions from the $O\ 1s\ 1a_1$ orbital are to a_1 , whose transition dipole moment, μ_{A_1} , is along the z axis, to b_2 , whose transition dipole moment, μ_{B_2} , is along the y axis, and to b_1 , whose transition dipole moment, μ_{B_1} , is along the x axis. In the observed spectra, these three dipole-allowed transitions, $A_1 \rightarrow A_1$, $A_1 \rightarrow B_1$ and $A_1 \rightarrow B_2$, are overlapped. Then the measured β values can be expressed as a weighted average of these three components:

$$\beta = \frac{\sigma_{A_1}\beta_{A_1} + \sigma_{B_1}\beta_{B_1} + \sigma_{B_2}\beta_{B_2}}{\sigma_{A_1} + \sigma_{B_1} + \sigma_{B_2}}, \quad (5)$$

where σ_{A_1} , σ_{B_1} and σ_{B_2} are the cross sections for the $A_1 \rightarrow A_1$, $A_1 \rightarrow B_1$ and $A_1 \rightarrow B_2$ transitions, respectively, and β_{A_1} , β_{B_1} and β_{B_2} are the anisotropy parameters of fragments originating from the $A_1 \rightarrow A_1$, $A_1 \rightarrow B_1$ and $A_1 \rightarrow B_2$ transitions, respectively.

Under the axial-recoil approximation, where one neglects the effect of molecular rotations on the dissociation, one can express the β_Λ value ($\Lambda = A_1, B_1$ and B_2) for the fragment ions in terms of the angle, χ_Λ , between the transition dipole moment, μ_Λ , and the direction of the velocity vector of the fragment [146–148]:

$$\beta_\Lambda = 2P_2(\cos \chi_\Lambda), \quad (6)$$

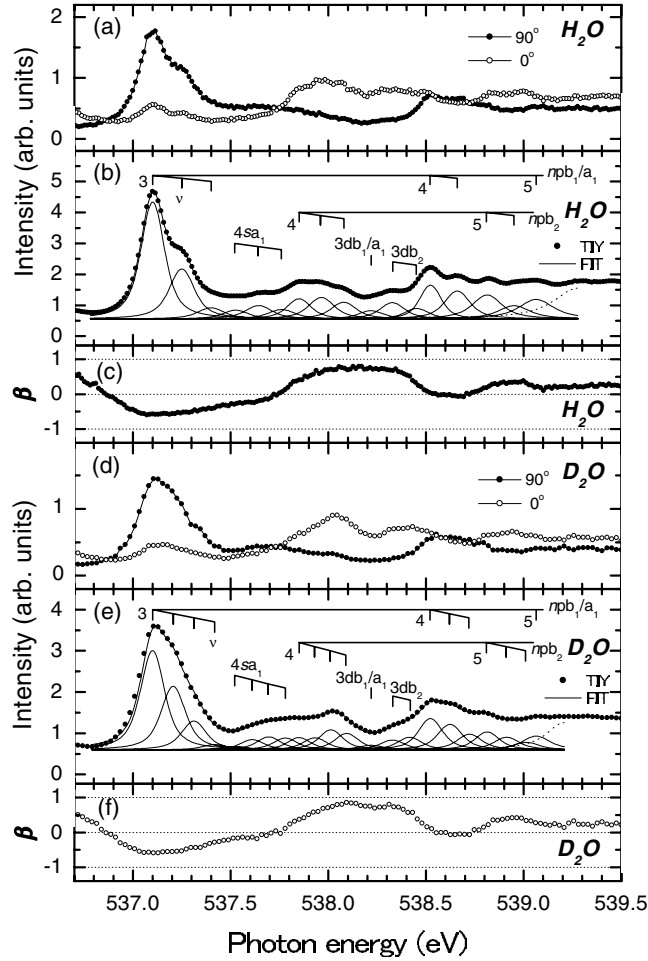


Figure 9. The yield spectra and the anisotropy parameter β of photofragment ions of H_2O (a)–(c) and D_2O (d)–(f) in the region of the O 1s $1a_1$ excitation to the Rydberg states. (a), (d) Yield spectra $I(0^\circ)$ and $I(90^\circ)$. (b), (e) Total ion yield spectrum (solid circles) and a fit to the spectrum (lines). (c), (f) The β values of the energetic (≥ 6 eV) ions. Statistical uncertainties are about the same as the size of the data points, as can be seen from the scatter of the points (from [15]).

where $P_2(\cos \chi_\Lambda) = (3 \cos^2 \chi_\Lambda - 1)/2$. Using this formula, one can estimate the β_Λ values for the $A_1 \rightarrow A_1$, $A_1 \rightarrow B_1$ and $A_1 \rightarrow B_2$ transitions to be $\beta_{A_1} = 0.12$, $\beta_{B_1} = -1$ and $\beta_{B_2} = 0.88$, respectively, from the stable geometry of the ground state H_2O , assuming that the molecular dissociation starts at the same molecular geometry as that of the ground state.

The $A_1 \rightarrow A_1$ transition ($\beta_{A_1} = 0.12$) appears both in $I(0^\circ)$ and $I(90^\circ)$, $A_1 \rightarrow B_1$ ($\beta_{B_1} = -1$) only in $I(90^\circ)$ and $A_1 \rightarrow B_2$ ($\beta_{B_2} = 0.88$) predominantly in $I(0^\circ)$. The measured β values include the contributions not only from the O 1s excitation but also from the ionization from the valence orbitals (see the baselines of the total ion yield curves in panels (b) and (e)). Based on the knowledge described above, the structures observed in the ion yield spectra can be assigned in the following manner.

The most prominent peak appears at 537.10 eV in the ion yield spectra of H_2O . This peak is significant in the ion yield spectrum $I(90^\circ)$, while it is weak in the $I(0^\circ)$ spectrum. The negative β value indicates that the dominant component of this peak is the $A_1 \rightarrow B_1$ transition.

The deviation of β from -1 , however, suggests that this peak cannot be ascribed to a single electronic transition, $A_1 \rightarrow B_1$, but should be ascribed to more than one overlapping electronic transition. This overlapping resonance is assigned as the promotion of the O 1s electron to the $3p_{a_1}$ and $3p_{b_1}$ orbitals. The $3p_{a_1}$ and $3p_{b_1}$ excited states may have slightly different energies according to the theoretical investigations [135, 162]. The energy difference is 110 meV by Schirmer *et al* [135] and 188 meV by Niu *et al* [162]. In the present high-resolution spectrum, a shoulder structure can be seen clearly on the higher-energy side (by ~ 150 meV) of this peak. This structure should, however, be attributed to the vibrational excitation with a_1 vibrational symmetry rather than to a different electronic state, because the behaviour of the angle-resolved ion yield curves (and thus the β curve) is similar to that of the prominent peak at 537.10 eV. In other words, the energy difference cannot be detected between the $3p_{a_1}$ and $3p_{b_1}$ excited states, even with the present energy resolution. According to the *ab initio* calculations for the O K-shell hole ionic state by Cesar *et al* [142], the energies for the symmetric stretching (a_1) and bending (a_1) vibrations are 448 and 166 meV, respectively. Therefore, the shoulder structure of the prominent peak can be ascribed to the excitation of the bending vibration. The second prominent peak in the $I(90^\circ)$ spectrum appears at 538.52 eV. The quantum defect estimated from the reported values for the O 1s ionization threshold [163] is similar to that for the most prominent peak at 537.10 eV, and thus can be assigned to $4p_{b_1}/4p_{a_1}$. This assignment also agrees with the *ab initio* calculations [135, 162].

In the ion yield spectrum $I(0^\circ)$, on the other hand, some additional broad features can be seen. The most prominent one is the broad maximum in the energy region 537.8–538.1 eV. This feature can be ascribed to $A_1 \rightarrow B_2$, because β has a large positive value ~ 0.6 in this region. Examining the quantum defect and referring to the *ab initio* calculations [135, 162], this band can be assigned as the excitation of O 1s electron to the $4p_{b_2}$ orbital. Another broad structure appears at ~ 538.3 eV, between $4p_{b_2}$ and $4p_{b_1}/4p_{a_1}$. The β value in this region is ~ 0.65 , and thus the structure can be ascribed to $A_1 \rightarrow B_2$. Examining the quantum defect (~ 0), this structure can be assigned to the excitation of the O 1s electron to the $3d_{b_2}$ orbital. According to the *ab initio* calculation [162], the O $1s \rightarrow 3d_{b_2}$ transition is indeed expected to have an oscillator strength comparable to those of $4p_{a_1}$ and $4p_{b_1}$.

A careful inspection reveals one weak and broad structure between the two prominent structures $3p_{b_1}/3p_{a_1}$ at 537.10 eV and $4p_{b_2}$ at ~ 538 eV. The structure is relatively clear in the total ion yield curves of figures 9(b) and (e). The β value is ~ 0 , and $I(0^\circ)$ and $I(90^\circ)$ are roughly parallel in this region. Thus the structure may be ascribed to $A_1 \rightarrow A_1$. According to the *ab initio* calculations [135, 162], the $4s_{a_1}$ level should be located between $3p_{b_1}/3p_{a_1}$ and $4p_{b_2}$, and the predicted oscillator strength is comparable to the one for $4p_{b_2}$. Therefore, this structure can be assigned to the excitation of the O 1s electron to the $4s_{a_1}$ orbital.

Quantitative data on the peak positions and on the vibrational energy spacings can be extracted from a simultaneous least-squares peak fitting to the entire ion yield spectra for H_2O and D_2O . Figure 9 includes the result of such peak fittings. The extracted quantitative information is presented in [15], together with further discussion.

4.2. Symmetry-resolved O 1s to Rydberg excitation spectra of CO_2

The CO_2 molecule is a linear molecule, which belongs to the $D_{\infty h}$ point group ($r(C-O) = 1.06 \text{ \AA}$) in the ground state, and the electronic configuration is

$$1\sigma_g^2 1\sigma_u^2 2\sigma_g^2 3\sigma_g^2 2\sigma_u^2 4\sigma_g^2 3\sigma_u^2 1\pi_u^4 1\pi_g^4 ({}^1\Sigma_g^+).$$

Here $1\sigma_g$ and $1\sigma_u$ are linear combinations of the two O 1s orbitals and $2\sigma_g$ is the C 1s orbital. Dipole-allowed absorption of the Σ_g ground state leads to the Σ_u and Π_u states. The dipole

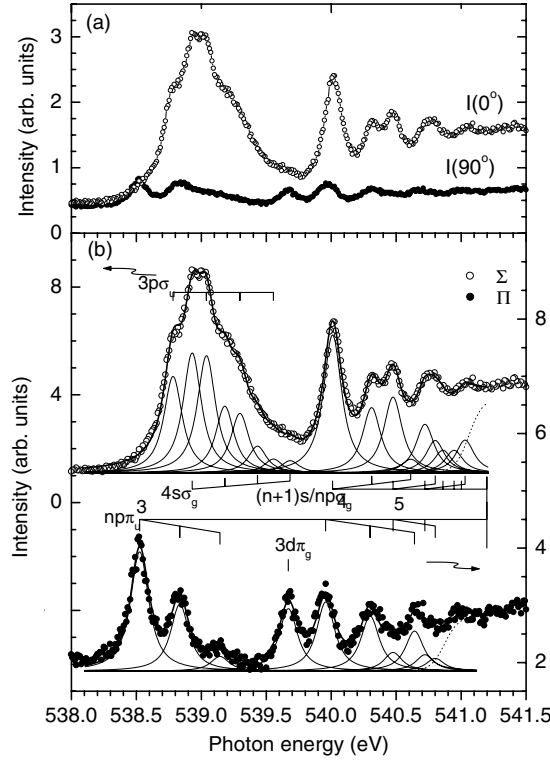


Figure 10. (a) Yield spectra, $I(0^\circ)$ and $I(90^\circ)$, for energetic fragment ions of CO_2 in the region of the O 1s excitation to the Rydberg states. (b) Symmetry-resolved spectra and the peak deconvolution analysis of the spectra (from [18]).

transition moments are parallel and perpendicular to the molecular axis for the $\Sigma_g \rightarrow \Sigma_u$ and $\Sigma_g \rightarrow \Pi_u$ transitions, respectively. There are three vibrational modes in the CO_2 molecule of the $D_{\infty h}$ point group: the symmetric stretching mode ν_1 of σ_g symmetry, the bending mode ν_2 of π_u symmetry and the antisymmetric stretching mode ν_3 of σ_u symmetry.

Figure 10(a) shows the yield spectra of the energetic ions (≥ 6 eV), $I(0^\circ)$ and $I(90^\circ)$, recorded in the 0° and 90° directions with respect to the \mathcal{E} vector [18]. Here the separation of the $\Sigma \rightarrow \Sigma$ and $\Sigma \rightarrow \Pi$ transitions is not perfect in the $I(0^\circ)$ and $I(90^\circ)$ spectra, partly because of the finite acceptance angles of the detectors, and partly because of the zero-point bending motion of the triatomic molecule.

The contamination can be eliminated by lowering the anisotropy parameters for the $\Sigma \rightarrow \Sigma$ and $\Sigma \rightarrow \Pi$ transitions, β_Σ and β_Π , respectively, under the condition that the statistically weighted average between β_Σ and β_Π is zero, i.e., $\beta_\Sigma + \beta_\Pi \times 2 = 0$. The prescription is as follows. The β values, which can be obtained from $I(0^\circ)$ and $I(90^\circ)$ using equation (4), can be expressed by a weighted average of the $\Sigma \rightarrow \Sigma$ and $\Sigma \rightarrow \Pi$ transitions:

$$\beta = \frac{\beta_\Sigma \sigma_\Sigma + \beta_\Pi \sigma_\Pi}{\sigma_t}, \quad (7)$$

where σ_Σ and σ_Π are the cross sections for the $\Sigma \rightarrow \Sigma$ and $\Sigma \rightarrow \Pi$ transitions, respectively, and $\sigma_t = \sigma_\Sigma + \sigma_\Pi$. From equation (7), one obtains

$$\sigma_\Sigma = \left(\frac{2}{3} \frac{\beta}{\beta_\Sigma} + \frac{1}{3} \right) \sigma_t \quad (8)$$

and

$$\sigma_{\Pi} = \left(\frac{1}{3} \frac{\beta}{\beta_{\Pi}} + \frac{2}{3} \right) \sigma_t. \quad (9)$$

Adjusting the β_{Σ} (β_{Π}) value so as to eliminate the contribution from the $\Sigma \rightarrow \Pi$ ($\Sigma \rightarrow \Sigma$) transition to the $I(0^\circ)$ ($I(90^\circ)$) spectrum, one can obtain the pure $\Sigma \rightarrow \Sigma$ ($\Sigma \rightarrow \Pi$) spectrum using the measured σ_t and β data. The resulting spectra are given by the open and solid circles in figure 10(b). Adopting the values $\beta_{\Sigma} = 1.6 (= -2\beta_{\Pi})$, one can see that the shoulder structure at 538.5 eV disappears in the $I(0^\circ)$ spectrum and a new band appears at 539.1 eV in the $I(90^\circ)$ spectrum. In this way one can obtain the symmetry-resolved spectra.

The peak positions, as well as the vibrational energy spacing and the intensity of each vibrational component, are extracted from a least-squares peak fitting to the symmetry-resolved spectra, the results of which are presented by the solid lines in figure 10(b).

Focus on the Π spectrum in figure 10(b). The first peak, at 538.53 eV, corresponds to the excitation to the $3p\pi_u$, because the effective principal quantum number of this peak is 2.26. The spacing between this peak and the second peak, at 538.83 eV, is 0.31 eV. This value is comparable to the frequency 307 meV [154] of the antisymmetric vibration for the O 1s ionized state in CO₂. Thus, it is reasonable to assign the peak at 538.83 eV to the vibrationally excited component (0, 0, 1) of $3p\pi_u$. Analogously, the peaks at 539.96 and 540.30 eV can be assigned to $4p\pi_u$ (0, 0, 0) and $4p\pi_u$ (0, 0, 1). Another prominent peak at 539.67 eV has the effective principal quantum number of 2.98. Thus, this peak is reasonably assigned to $3d\pi_g$.

Note that all the observed vibrational components are attributed to the antisymmetric stretching mode ν_3 . The vibrational structure in the absorption spectra is usually due to excitation of totally symmetric modes, i.e., symmetric stretching mode ν_1 in the case of CO₂. The excitation of the antisymmetric stretching mode ν_3 is optically forbidden in the absence of the vibronic coupling. The excitation of the O 1s inner-shell electron, however, leads to symmetry lowering, as a consequence of vibronic coupling, which mixes the nearly degenerate states O 1s $1\sigma_g^{-1}np\pi_u$ and O 1s $1\sigma_u^{-1}np\pi_u$. As a result, the antisymmetric stretching vibration, ν_3 , is excited in the inner-shell excited states.

We now discuss the $\Sigma \rightarrow \Sigma$ spectrum in figure 10(b), focusing on the feature observed at 538.7–539.7 eV. With the resolving power of 7000, it is not possible to observe the vibrational structure in this band [164]. Even with the resolving power of 10 000, it is nearly impossible to assign all the vibrational structures of this band without resolving the symmetry of the excited states experimentally [4]. In the symmetry-resolved spectrum at the resolving power of 14 000, however, two vibrational progressions starting at 538.78 and 538.93 eV, with vibrational frequencies 250–255 meV, can be extracted unambiguously. These progressions can be attributed to those of the antisymmetric stretching vibrations, ν_3 , associated with two electronic states, $3p\sigma_u$ and $4s\sigma_g$. Transitions to the higher Rydberg orbitals are also observed and assigned to higher members, $np\sigma_u$ and $(n+1)s\sigma_g$, as shown in figure 10(b).

Generally, vibrational progressions are observed when the stable geometries of the molecule are different between the ground and excited states. Thus, one can extract the information on the geometry of the inner-shell excited molecule from the measured peak positions and intensity distributions of the excited vibrations, employing the linear coupling model. This model was originally proposed by Cederbaum and Domcke [165], and has been used successfully in the analyses of the vibrational structures in the photoelectron spectra [166–168]. The extension of this model to include the antisymmetric stretching mode accompanied by the lowering of symmetry has also been done by Domcke and Cederbaum [150].

In the linear coupling model, the harmonic oscillator approximation is employed to express the electronic initial and final states of the transition, and furthermore the vibrational frequencies of the initial and final states are assumed to be identical. Then the Franck–Condon

factors for the excitation from $v = 0$ in the electronic ground state to the v' vibrational components of the electronic excited state are given by a Poisson distribution:

$$I(0 \rightarrow v') = e^{-S} \frac{S^{v'}}{v'!}. \quad (10)$$

The S factor can be regarded as an average vibrational quantum number for the vibrational excitation. Within the harmonic oscillator approximation, one can show in the present case that

$$S = \frac{K}{2\hbar\omega_3} (\Delta r)^2, \quad (11)$$

where K is the force constant for the antisymmetric stretching vibration mode ν_3 , ω_3 is the frequency of the ν_3 vibration in the ground state ($\omega_3 = 291$ meV) and Δr is the change of the C–O bond lengths between the initial and final states. One can approximately take account of the change in the frequency between the initial and final states by using the force constant, K , for the final state [167]. Then the change of the C–O bond lengths Δr can be expressed by

$$\Delta r = \left(\frac{2S\hbar}{\omega_3} \frac{m_C + 2m_O}{m_C m_O} \right)^{1/2} \frac{\omega_3}{\omega'_3}, \quad (12)$$

where ω'_3 is the frequency of the antisymmetric stretching vibration for the excited state and m_C and m_O are atomic masses for carbon and oxygen, respectively.

The intensity ratio (0,0,0):(0,0,1):(0,0,2) of the $3p\pi_u$ band extracted from the peak fitting is 59:34:7. Using equation (10), one obtains $S = 0.54$. Inserting this into equation (12) one receives $\Delta r = 0.056$ Å. This value is in good agreement with $\Delta r = 0.055$ Å, reported by Kivimäki *et al* [154] for the O 1s ionized state of CO₂. Note that the increase in the vibrational frequency from $\omega_3 = 291$ meV in the ground state to $\omega'_3 = 310$ meV in the excited state corresponds to the increase in the bond strength in the final state. Thus, one can expect that the bond lengths are reduced by 0.056 Å in the $3p\pi_u$ inner-shell excited state. Analogously, one finds that the C–O bond lengths are elongated by 0.096 and 0.075 Å for $3p\sigma_u$ and $4s\sigma_g$, respectively.

4.3. Symmetry-resolved C 1s $\rightarrow 2\pi_u$ excitation spectra of CO₂

As can be seen in figure 8, the bending motion proceeds in the direction parallel to the electric vector \mathcal{E} of the incident light in the A_1 state and perpendicular to \mathcal{E} in the B_1 state. In the angle-resolved ion yield spectroscopy, one detects fragment ions in the directions parallel (0°) and perpendicular (90°) to \mathcal{E} . The C 1s $\rightarrow 2\pi_u$ excitation takes place preferentially for the molecules with molecular axes aligned in the direction perpendicular to \mathcal{E} . The fragment ions from the linear CO₂ molecule are detected only by the detector at 90°. Therefore, the detection of the fragment ions by the detector at 0° directly reflects the bending motion of the molecule. The bending motion (the displacement of the C atom) is in the direction parallel to the transition dipole moment μ_{A_1} for the A_1 state and perpendicular to the transition dipole moment μ_{B_1} for the B_1 state. Thus, the ions originated from the B_1 excitation cannot be detected at 0°.

We introduce here the quantities $I(0^\circ)$ and $I(90^\circ)$ for ion yields recorded by the 0° and 90° detectors, respectively, and $I(A_1)$ and $I(B_1)$ for ion yields originated from the A_1 and B_1 excitations, respectively. These quantities are normalized in such a way as to satisfy the following relation:

$$I(A_1) + I(B_1) = I(0^\circ) + 2 \times I(90^\circ). \quad (13)$$

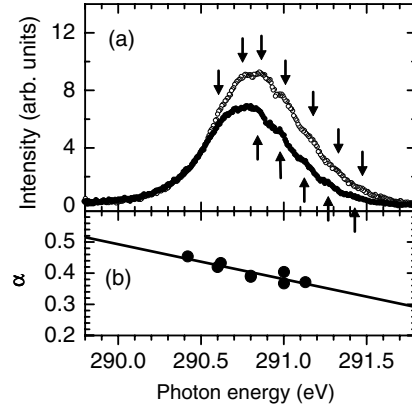


Figure 11. (a) Angle-resolved energetic-ion yield spectra of CO_2 , measured across the $\text{C } 1s \rightarrow 2\pi_u$ resonance. Closed and open circles represent $I(0^\circ)$ and $I(90^\circ)$, respectively. (b) Photon-energy dependence of the α factor (see text) (from [17]).

Because $I(0^\circ)$ does not include the contribution from the B_1 excitation, one can express $I(0^\circ) = \alpha \times I(A_1)$, with α being a branching ratio of $I(A_1)$ to $I(0^\circ)$. Then $I(A_1) = I(0^\circ)/\alpha$ and

$$I(B_1) = 2 \times I(90^\circ) - \frac{1 - \alpha}{\alpha} \times I(0^\circ) \quad (14)$$

follow. Thus, one can extract $I(A_1)$ and $I(B_1)$ from $I(0^\circ)$ and $I(90^\circ)$ if we know the value of α . The value of α , on the other hand, can be related to the ratio $r \equiv I(A_1)/[I(A_1) + I(B_1)]$ in the following manner:

$$\alpha = \frac{I(0^\circ)}{r \times [I(0^\circ) + 2 \times I(90^\circ)]}. \quad (15)$$

The values of r can be measured by means of the triple-ion-coincidence momentum-imaging technique described later. Thus, we can extract $I(A_1)$ and $I(B_1)$ from the measurements of $I(0^\circ)$ and $I(90^\circ)$.

Figure 11(a) presents the angle-resolved yield spectra of ions with energy ≥ 6 eV, measured across the $\text{C } 1s \rightarrow 2\pi_u$ resonance of CO_2 [17]. The monochromator bandwidth employed here is ~ 30 meV. The spectra are presented after subtraction of the baselines, which include contributions from the valence ionization and the ionization by the second-order light. Vibrational structure can be observed in both $I(0^\circ)$ and $I(90^\circ)$, as indicated by arrows in the figure. Careful inspections, however, reveal that the vibrational structures observed in $I(0^\circ)$ and $I(90^\circ)$ are slightly different.

The values of α can be obtained from the values of r measured at several energies across the $\text{C } 1s \rightarrow 2\pi_u$ resonance and $I(0^\circ)$ and $I(90^\circ)$ measured at the same energies, using equation (15), and are plotted in figure 11(b). The values of α exhibit weak energy dependence, and thus are fitted by a linear line. Finally, symmetry-resolved excitation spectra, $I(A_1)$ and $I(B_1)$, have been extracted from α , $I(0^\circ)$ and $I(90^\circ)$.

Figures 12(a) and (c) show the symmetry-resolved excitation spectra $I(A_1)$ and $I(B_1)$, respectively. Only one vibrational progression appears in the $I(B_1)$ spectrum. One can also recognize one vibrational progression on the high-energy side of the $I(A_1)$ spectrum. The vibrational spacings are ~ 145 meV for both progressions: the peaks appear at different energies in the $I(A_1)$ and $I(B_1)$ spectra. The $I(B_1)$ spectrum in figure 12(c) is well described by overlapping seven Voigt profiles, whose Gaussian and Lorentzian widths are 30 and 170 meV,

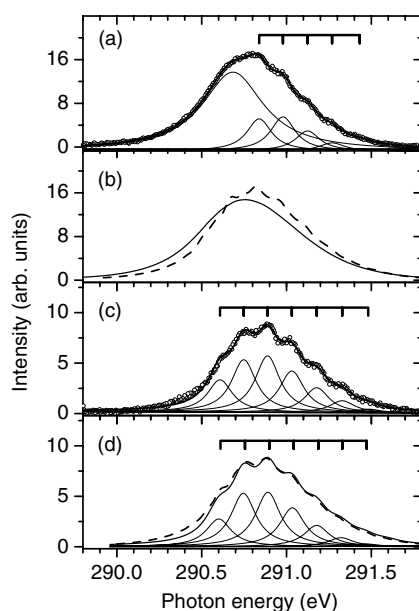


Figure 12. Symmetry-resolved excitation spectra of CO₂. (a), (c) Experimental excitation spectra $I(A_1)$ and $I(B_1)$, respectively. Thick solid curves, the results of the fitting with some Voigt profiles given by the thin solid curves. (b), (d) Theoretical excitation spectra $I(A_1)$ and $I(B_1)$, respectively. Thick solid curves, the spectra calculated in the adiabatic representation. Thin solid curves in (d), contributions from each vibrational component. Dashed curves, the spectra calculated taking account of the non-adiabatic effect, using a simple approximation, see the text for details (from [17]).

respectively. The $I(A_1)$ spectrum in figure 12(a), on the other hand, is well described by one broad component, whose Gaussian and Lorentzian widths are 30 and 440 meV, respectively, and five narrow lines, whose Gaussian and Lorentzian widths are 30 and 170 meV, respectively.

At first glance, one may consider the observed vibrational progression as the symmetric stretching mode, $(\nu_1, 0)$, in both A_1 and B_1 states. Note, however, that one can expect that the A_1 state is bent and thus the bending vibration should be highly excited. The frequency of the bending vibration is ~ 100 meV [51, 161], and lower in the Franck–Condon region where the excitation takes place. Thus, the vibrational spacing is comparable with the natural lifetime width, $\Gamma \sim 95$ meV, of the C K-shell hole state [20]. These facts may explain why the vibrational structure is not resolved on the lower-energy side of the $I(A_1)$ spectrum. If this is the case, however, one cannot expect to see the vibrational structure on the higher-energy side either. Note also that the Lorentzian width of 170 meV obtained by the fitting is significantly larger than expected.

To answer the questions raised above, the excitation spectra have been simulated by using *ab initio* potential energy surfaces of the inner-shell excited state [17]. In the calculations, the point group of the molecule is assumed to be C_{2v} . The symmetric stretching and bending modes are taken into account, but the antisymmetric stretching mode is neglected.

Figure 12(d) shows the theoretical $I(B_1)$ spectrum together with each vibrational component: each component is described by a Lorentzian profile with the width of 180 meV. The theoretical calculation confirms that the observed progression is indeed the progression $(\nu_1, 0)$ of the symmetric stretching mode ν_1 . The calculated $I(A_1)$ spectrum is presented in figure 12(b). Each vibrational component (not shown in the figure) is described by the

Lorentzian profile with the width 180 meV as in figure 12(d). The theoretical calculation reproduces the global broad feature well but does not reproduce the vibrational structure, because of the dense vibrational components of the highly excited bending mode, as expected. Changing the Lorentzian width to ~ 100 meV does not change the result significantly.

In order to explain the vibrational structure observed in the $I(A_1)$ spectrum and unexpected large Lorentzian widths in both $I(A_1)$ and $I(B_1)$ spectra, one should take account of the non-adiabatic coupling between the A_1 and B_1 states neglected in the theoretical calculation. This non-adiabatic effect, referred to as the dynamical Renner–Teller effect [159], is caused by the coupling between the bending nuclear motion and the electronic motion. Then, the vibronic eigenstates are in principle obtained by solving the Schrödinger equation including the non-adiabatic coupling term. Taking account of contributions of the non-adiabatic coupling only qualitatively, by using a very simple approximation and assuming that the vibronic states are roughly represented in terms of a combination of the A_1 and B_1 adiabatic eigenstates, the excitation spectrum may be approximated by a weighted sum of the $I(A_1)$ and $I(B_1)$ spectra calculated in the adiabatic representation, by shifting the energies slightly away from one another. Figure 12(b) presents the $I(A_1)$ spectrum (dashed curve), calculated as the sum of the adiabatic $I(A_1)$ and $I(B_1)$ spectra weighted with the ratio of $A_1:B_1 \sim 1:0.2$. The calculation taking account of the vibronic coupling in this way reproduces the experimental $I(A_1)$ spectrum well, and illustrates that the vibrational structure in the $I(A_1)$ spectrum originates from the symmetric stretching mode in the B_1 state. Figure 12(d) presents the $I(B_1)$ spectrum (dashed line), calculated in a similar way. The calculation reproduces the observed spectrum well. The Lorentzian widths adopted in these calculations are not 180 meV but 110 meV, illustrating that the apparent broadening of the Lorentzian component in the experimental spectra is mostly due to the overlap of the broad component originating from the adiabatic $I(A_1)$ spectrum.

5. Resonant photoemission spectroscopy

Resonant photoemission spectroscopy, or resonant Auger spectroscopy, of atoms and molecules is the field that benefits significantly from the development of the third-generation SR sources and high-resolution soft-x-ray monochromators installed there. Indeed, a number of papers have already been published, as briefly reviewed in section 1. Here, only two examples, one for Ne [35, 48] and the other for H_2O [68], are described. In these two examples, Doppler broadening due to thermal motion of the sample gases is the main source of spectral resolution.

The resonant Auger spectra of Ne were observed previously at moderate resolutions, without resolving multiplet structures [38, 47, 127, 169]. In the following subsection, it is shown that the Ne^+ Auger final states $2p^{-2}(^1D_2)3p\ ^2P$, 2D and 2F can be resolved at the overall experimental width of 100–130 meV [35] and that measurements of partial cross sections for these states reveal that not only the interference between the direct and resonant channels, but also the interference among the resonances, is important in describing dramatic changes of the branching ratios to these states [48].

The resonant Auger spectra of H_2O were recorded at the $O\ 1s \rightarrow 4a_1$ excitation at MaxII [56], exhibiting clear evidence of ultrafast dissociation before the Auger decay. Here, we focus on the $O\ 1s \rightarrow 2b_2$ excitation (see figures 5 and 6). It is shown that the two-dimensional nuclear motion in the Auger final state can be probed by means of resonant Auger spectroscopy and, furthermore, that it can be mediated by sampling a different portion of the potential curve and changing the nuclear motion in the inner-shell excited state [68].

Finally, it is shown that Doppler broadening is reduced significantly and the spectral widths nearly reach the Doppler-free limit, by use of a well collimated molecular beam, for both samples Ne and H_2O [128].

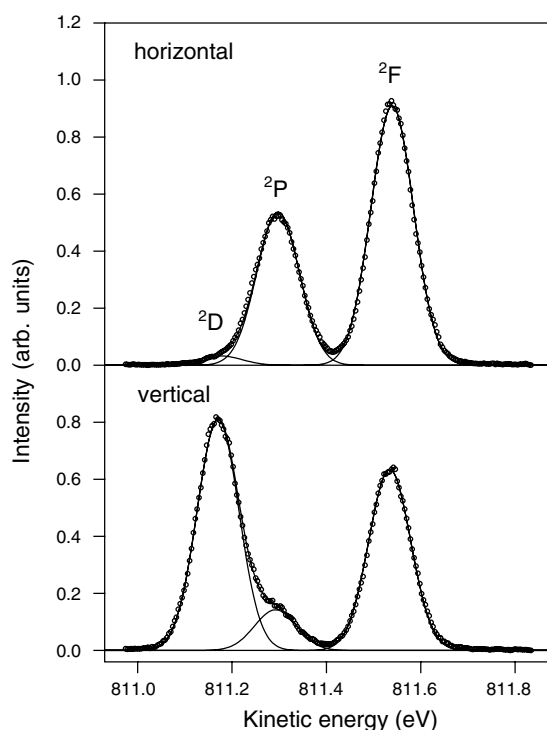


Figure 13. A part of the electron spectra of the resonant Auger transitions from the $\text{Ne } 1s^{-1}3p$ state to the final Ne^+ of the $2p^{-2}(^1D_2)3p$ 2D , 2P and 2F states, recorded at a photon energy of 867.12 eV, with horizontal (upper) and vertical (lower) polarizations (from [35]).

5.1. Interference effects in resonant photoemission of Ne

Figure 13 shows a portion of the electron spectra of the spectator Auger transitions from the $\text{Ne } 1s^{-1}3p$ state to the final $\text{Ne}^+2p^{-2}(^1D_2)3p$ 2P , 2D and 2F states [35]. The spectra were recorded at a photon energy of 867.12 eV, for horizontal (upper) and vertical (lower) polarizations. The analyser was operated at pass energy 20 eV, resulting in the analyser bandwidth of ~ 13 meV. The spectra were well fitted to the three Gaussian profiles of ~ 105 meV FWHM, as shown in figure 13. Gaussian profiles were chosen because in the electron spectra the broadening caused by instrumental and Doppler effects was much larger than the natural lifetime width of the Auger final states. The experimental width of ~ 105 meV is indeed a convolution of the three Gaussian components: the monochromator bandwidth of ~ 66 meV, the analyser bandwidth of ~ 13 meV and the Doppler width of 79 meV, due to thermal motion of the Ne atoms.

The branching ratio for the $2p^{-2}(^1D_2)3p$ 2P , 2D and 2F final states, as well as the anisotropy parameters β , was extracted from several spectra, similar to those in figure 13. The branching ratio is $0.18 \pm 0.01 : 0.35 \pm 0.02 : 0.47 \pm 0.02$ for $^2P : ^2D : ^2F$ and nearly the same as the statistical ratio $0.2:0.33:0.47 (=3:5:7)$. The β values are 0.98 ± 0.07 , -0.95 ± 0.06 and 0.27 ± 0.05 for 2P , 2D and 2F , respectively. These values are in good agreement with the predicted values 1.0, -1.0 and 0.286 for 2P , 2D and 2F , respectively, based on the spectator model within the LSJ -coupling scheme, where the electron wave is restricted to the d wave.

Electron emission to the $2p^4(^1D_2)3p$ 2P , 2D and 2F states was also measured at various photon energies in the 1s excitation region, with the monochromator band width of ~ 66 meV and analyser bandwidths of ~ 33 meV [48]. Note that the analyser bandwidth was set to a

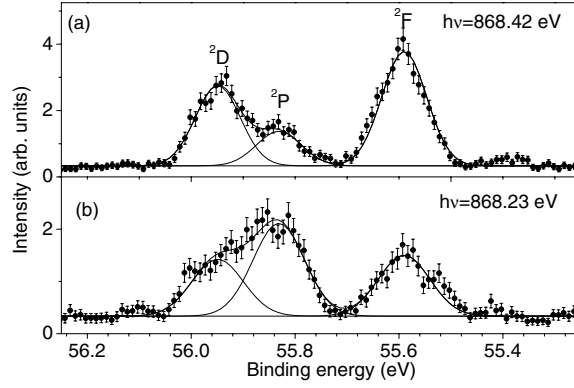


Figure 14. Angle-integrated electron spectra measured at the photon energies of (a) 868.42 and (b) 868.23 eV, together with the fit by Gaussian profiles (from [48]).

larger value than that in figure 13. The angle-integrated spectra were obtained from the 0° - and 90° -spectra, after correction for photon flux intensity and degrees of linear polarization (see [41] for a general procedure). At photon energies where the electron count rates were low, the acquisition time was increased, so that measurements at all photon energies had enough statistics to extract the line strengths with sufficiently small uncertainties. Figure 14 shows two examples of angle-integrated electron spectra recorded at two photon energies close to the energy for the minimum of the cross section between the 3p and 4p resonances [48]. The error bars contain the statistical contributions as propagated from the number of counts in the original spectra. From spectra similar to figure 14, the line strength of each component was extracted as a function of photon energy, by a least-squares fit with Gaussian profiles. In the fit for each electron spectrum, the separations between the states were fixed at the values obtained at the peak of the 3p resonance [35] (see figure 13). The partial cross sections thus measured are displayed in figure 15(a) [48]. All the resonances show nearly symmetric profiles in every partial cross section. Close inspections, however, reveal that the resonance exhibits slightly different asymmetric profiles for different partial cross sections. The relative branching ratios obtained from the measured partial cross sections exhibit dramatic oscillations typical of interference effects, as can be seen in figure 15(b).

Using the model of Kabachnik and Sazhina [170] (see also [171]), the amplitude for each specific channel α in the region of one isolated resonance is written as follows:

$$A_\alpha = d_\alpha + \mathcal{D}_\alpha \frac{q + \epsilon}{i + \epsilon}, \quad (16)$$

where d_α and \mathcal{D}_α represent the amplitudes of the direct and resonant processes. Equation (16) can be generalized to the case of more than one resonance in the following way:

$$A_\alpha = d_\alpha + \sum_m \mathcal{D}_{m\alpha} \frac{q_m + \epsilon_m}{i + \epsilon_m}. \quad (17)$$

Note that q in equation (16) is the same as in equation (3). Following the result that the resonance profiles in the total cross section σ are symmetric (i.e., $q_m \rightarrow +\infty$ and $\mathcal{D}_{m\alpha} = q_\alpha \mathcal{D}_{m\alpha}$ where $\mathcal{D}_{m\alpha}$ is related to the dipole moment of the resonance excitation), equation (17) can be replaced by

$$A_\alpha = d_\alpha + \sum_m \frac{\mathcal{D}_{m\alpha}}{i + \epsilon_m}. \quad (18)$$

In this model each channel α is defined by the final ionic state j and by the angular momentum l of the outgoing electron, $\alpha \equiv (j, l)$, as in [170]. We assume the LSJ -coupling scheme.

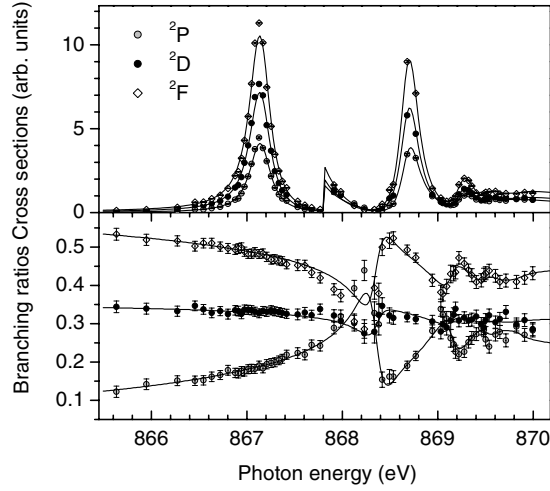


Figure 15. (a) Measurements of the partial cross sections of $2p^4(^1D_2)3p$, together with the fit of individual components. (b) Branching ratios extracted from the measured electron spectra (points), and from the corresponding fit (curves) (from [48]).

Then, each partial cross section, σ_j , corresponds to the incoherent sum of the two different photoelectron channels, $l = 0, 2$. Thus, each partial cross section is parametrized as follows:

$$\sigma_j = A_j + B_j \sum_m \frac{R_m^2}{1 + \epsilon_m^2} + \sigma_{\text{dir-res},j} + \sigma_{\text{res-res},j} + \sigma_{1s,j}, \quad (19)$$

with R_m normalized so that R_{3p} is unity. The direct-resonant, $\sigma_{\text{dir-res},j}$, and resonant-resonant, $\sigma_{\text{res-res},j}$, interference terms are given as follows:

$$\sigma_{\text{dir-res},j} = 2C_j \sum_m \frac{R_m \epsilon_m}{1 + \epsilon_m^2}, \quad (20)$$

and

$$\sigma_{\text{res-res},j} = 2B_j \sum_{m < n} \frac{R_m R_n (1 + \epsilon_m \epsilon_n)}{(1 + \epsilon_m^2)(1 + \epsilon_n^2)}. \quad (21)$$

A_j , B_j and C_j are defined as

$$A_j = \sum_{l=0,2} d_{j,l}^2, \quad (22)$$

$$B_j R_m R_n = \sum_{l=0,2} D_{m,j,l} D_{n,j,l}, \quad (23)$$

$$C_j R_m = \sum_{l=0,2} d_{j,l} D_{n,j,l}. \quad (24)$$

$\sigma_{1s,j}$, described by the same analytic form as equation (2), expresses the contributions from high $1s^{-1}np$ ($n \geq 9$) members as well as from the $1s$ ionization.

The electron spectra recorded at the peak of each resonance show almost the same branching ratios, close to the statistical ratios expected within the LSJ -coupling scheme: $B_{2P}:B_{2D}:B_{2F} = 3:5:7$. We thus assume that different resonances have the same branching ratios over different final states. This makes B_j well defined in equation (23). In general, from equations (22)–(24), A_j , B_j , C_j are constrained to fulfil the triangular inequality $C_j^2 \leq A_j B_j$.

However, by using the spectator model within the LSJ -coupling scheme, the photoelectron wave is restricted to $l = 2$ and then $C_j^2 = A_j B_j$.

The partial cross sections in figure 15(a) are fitted simultaneously using the model described above. In the fitting, the profiles (19) are broadened by convolution with a Gaussian distribution, with FWHM fixed to 66 meV to simulate the monochromator bandwidth. As can be seen in figure 15(a), the fit reproduces the measurements well. The continuous lines superimposed on the measured branching ratios in figure 15(b) are not the results of an additional fit, but the branching ratios calculated from the three simultaneous fits for the partial cross sections in figure 15(a). The agreement between the continuous lines and the experimental points is reasonable.

Consider how the interference plays the role of describing the oscillations in the branching ratios. If the direct ionization process is absent for all the channels, the branching ratios to the $\text{Ne}^+2p^{-2}(^1D_2)3p\ ^2P$, 2D and 2F states become constant in the present model. If the direct process is present, then the energy for the minimum of the cross section varies, depending on the ratio between A_j and B_j . Thus it is clear that the direct–resonant interference term is essential in describing the oscillations of the branching ratios. On the other hand, if the resonant–resonant interference term is switched off, each partial cross section does not go close to zero any more in the inter-resonance regions, and thus the amplitudes of the oscillations are significantly suppressed. Indeed, attempts to fit the partial cross sections with the incoherent sum of the Fano-like profile (3) fail to reproduce the large oscillations of the branching ratios in the inter-resonance regions. This is a clear indication that the $\sigma_{\text{res-res}}$ terms are important, i.e., the resonances are not isolated.

5.2. Probing nuclear motion in the Auger final state in H_2O^+

Some of the electron spectra recorded at various photon energies across the $\text{O } 1s \rightarrow 2b_2$ resonance of H_2O are presented in figure 16 [70]. The spectra in figure 16 cover the binding energy range of the three photoemission bands X $1b_1^{-1} \ ^2B_1$, A $3a_1^{-1} \ ^2A_1$ and B $1b_2^{-1} \ ^2B_2$. From figure 16, the resonance enhancement of electron emission due to participator Auger decay is evident for the X and B bands.

The monochromator bandwidth was ~ 40 meV and the bandwidth of the electron analyser was ~ 33 meV. The Doppler width due to thermal motion of the sample molecule is ~ 70 meV. Unresolved rotational structure may add an additional contribution to the line broadening. The slow drift of the photon energy (< 20 meV) during the measurements, caused by the gradual change in temperature of the optics due to the heat load, may also add additional line broadening. The bottom spectrum (a) was recorded at the foot of the $\text{O } 1s \rightarrow 2b_2$ resonance. The intensity was multiplied by six. One can see clear vibrational structure neither in the A band nor in the B band. Spectra (b) and (c) were recorded on the low-energy side of and on top of the (0, 0) component, respectively, and spectra (d) and (e) were recorded at the peaks of the (1, 0) and (2, 0) components, respectively.

Focus on the X band. The progression of the symmetric stretching vibrations with the vibrational spacing ~ 400 meV is clearly observed. The enhancement of the higher vibrational components ($v_1, 0$) with $v_1 \geq 3$ in the X band becomes significant when higher vibrational components ($v_1, 0$) with $v_1 \geq 1$ are excited in the $\text{O } 1s^{-1}2b_2$ state. Note that, if the lifetime of the inner-shell excited state were zero, the vibrational distribution should have coincided for all the spectra. The symmetric stretching vibration is, however, more excited in the X state when it is populated by the resonant Auger process via the higher vibrational component of the inner-shell excited state. The reason for this is found in the fact that the symmetric stretching motion proceeds in the inner-shell excited state before vibrational energy is transferred to the Auger final state.

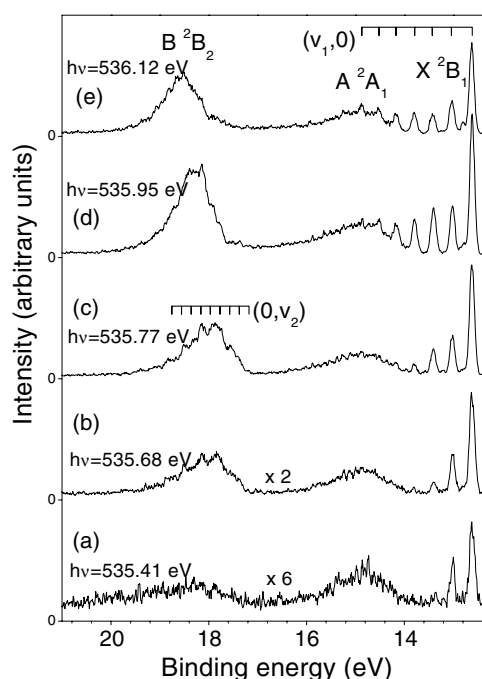


Figure 16. Electron spectra of H₂O to the X $1b_1^{-1}2B_1$, A $3a_1^{-1}2A_1$ and B $1b_2^{-1}2B_2$ states at various excitation energies across the O $1s \rightarrow 2b_2$ band. Photon energies are given in the figure (from [70]).

Turn your attention to the B band. Reutt *et al* [172] reported the vibrational frequencies of 375 and 203 meV for symmetric stretching (ν_1) and bending (ν_2) modes, respectively. In the case of direct photoemission, both modes are highly excited [172], exhibiting a very broad band structure (spectrum (a) in figure 16, where no vibrational structure could be resolved). When the B state is populated by the resonant Auger process via the O $1s \rightarrow 2b_2$ (0, 0) excitation, the vibrational structure can be resolved (see spectra (b) and (c)), and exhibits spacing of ~ 200 meV. Thus most of the observed vibrational structure may be attributed to the ν_2 mode. The vibrational structure becomes less resolved at the O $1s \rightarrow 2b_2$ (1, 0) excitation (spectrum (d)) and at the (2, 0) excitation (spectrum (e)). The band peak appears at higher binding energy when the excitation energy is increased, indicating that higher vibrational components are excited in the Auger final state. The disappearance of the vibrational structure may be attributed to the excitation of both the ν_1 and ν_2 modes.

To analyse the Auger spectra, a series of *ab initio* calculations have been carried out for potential energy surfaces of the ground state, the O $1s^{-1}2b_2$ inner-shell excited state and the B $1b_2^{-1}$ Auger final state [68]. Figure 17 presents a comparison between the experimental and theoretical results of electron emission spectra in the binding energy region of the B band. The theoretical spectra are calculated employing the lifetime vibrational interference theory [173] and then convoluted with a Gaussian profile of FWHM = 105 eV (dashed curves). The global features are in good accord with the experimental observations. The stick bars represent vibrational components in the B $1b_2^{-1}$ Auger final state. The intensity distributions of the vibrational components dramatically change, depending on the excitation energy. For the sake of convenience, some representative vibrational components are labelled with numbers, which represent the order of the vibrational eigenstates of the B $1b_2^{-1}$ Auger final state.

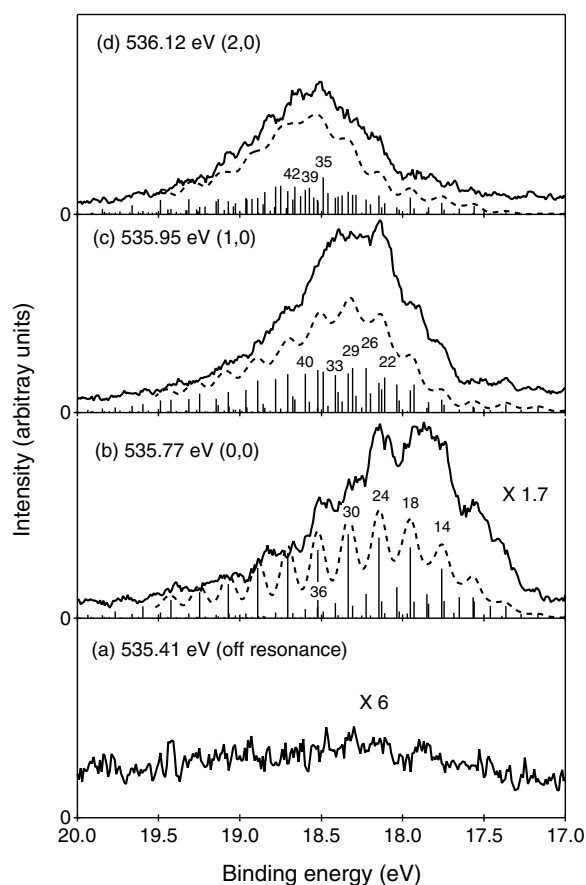


Figure 17. Measured (solid) and calculated (dashed) resonant Auger spectra of H₂O to the $1b_2^{-1}$ Auger final state at four excitation energies across the O $1s \rightarrow 2b_2$ band. Photon energies and corresponding vibrational components in the inner-shell excited state are also displayed. The vertical bars represent the calculated vibrational components (from [68]).

Focus on the excitation to the (0, 0) component (see figure 17(b)). Examining the wavefunctions, the vibrational component 24 is assigned to $(v_1, v_2) = (0, 7)$ and the component 30 to (0, 8). The equilibrium H–O–H angle ($\sim 57^\circ$) of the Auger final state B $1b_2^{-1}$ is much smaller than that of the inner-shell excited state ($\sim 100^\circ$). Thus the bending vibrations are highly excited in the Auger final state, via the inner-shell excitation. It is confirmed that the other main components are also attributed to $(0, v_2)$.

Similar to the experimental observations, the vibrational structure of the calculated decay spectra becomes less resolved when the photon energy is increased. This is because not only the dominant v_2 mode but also the v_1 mode are excited. Components 26 and 35 in figures 17(c) and (d) are attributed to (1, 6) and (2, 6), respectively. It is found that vibrational progressions $(1, v_2)$ and $(2, v_2)$ are preferentially excited by the resonant Auger processes following the excitations at 535.95 and 536.12 eV. This may be a natural consequence of the fact that the $O1s^{-1}2b_2$ inner-shell excited state and the $1b_2^{-1}$ Auger final state have similar equilibrium bond distances, and thus the vibrational energy of the v_1 mode in the inner-shell excited state is directly transferred to the Auger final state.

The key point is that this mode selectivity decreases when the excitation energy is increased. With the excitation of $O\ 1s^{-1}2b_2\ (1, 0)$, in addition to the $(1, \nu_2)$ main progression, one can also identify $(0, \nu_2)$ and $(2, \nu_2)$ in the $1b_2^{-1}$ Auger final state. With the excitation to $O\ 1s^{-1}2b_2\ (2, 0)$, the intensity of the $(2, \nu_2)$ components in the $1b_2^{-1}$ Auger final state is comparable to the other components. As a result, many more vibrational components pile up to form the unresolved band that can be seen in figure 17(d). The reason can be found in the analysis of the wavefunctions. Symmetric stretching and bending motions in the Auger final state are not completely separated in the region where the vibrational wavefunctions overlap with those of the inner-shell excited state. The ν_1 and ν_2 modes in the inner-shell excited state also have both symmetric stretching and bending character. These two modes are, however, significantly different in the inner-shell excited state and in the Auger final state. As a result, the ν_1 mode caused in the inner-shell excited state can be transferred not only to the ν_1 mode but also to the ν_2 mode in the Auger final state. In this way, complex two-dimensional nuclear motion is mediated in the Auger final state by the resonant Auger emission process via the $(\nu_1, 0)$ components in the inner-shell excited state.

5.3. Towards Doppler-free resonant Auger spectroscopy

Note that the spectral widths of the resonant Auger spectra shown in the previous subsections are dominated by the contributions of the Doppler broadening due to thermal motion of the sample atoms and molecules in the gas phase. In this subsection, we describe a trial of suppressing the Doppler broadening effects. The apparatus consists of a high-resolution electron spectrometer (Gammadata-Scienta SES-2002) and a molecular beam source (MB Scientific MBS JD-01) [128]. The molecular beam source reduces deterioration of resolution due to the Doppler effects in gas-phase electron spectroscopic experiments. The original vibrational and rotational distributions in the gas sample are conserved since no expansion cooling occurs. The beam device has an orifice of $1\text{ mm} \times 8\text{ mm}$, covered by a 1 mm thick micro-channel plate. A multi-channel array permits a much higher target pressure than a single-tube device. The inlet pressure of an effusive beam source is limited roughly to 1 Torr, i.e., the level where the mean free path regarding intermolecular collisions equals the channel length.

Figure 18 presents the same portion of the electron spectra of Ne as figure 13. The analyser is operated at the pass energy of 50 eV, resulting in the analyser bandwidth of $\sim 33\text{ meV}$. The spectra are well fitted to the three Gaussian profiles of 74 meV FWHM as shown in figure 18. The experimental width of 74 meV corresponds to a convolution of the analyser bandwidth $\sim 33\text{ meV}$ and the monochromator bandwidth $\sim 66\text{ meV}$. This experimental width should be compared with the experimental width of previous observation with a gas-cell (figure 13), where the observed width 105 meV corresponds to the convolution of the monochromator bandwidth of $\sim 66\text{ meV}$, the analyser bandwidth of $\sim 13\text{ meV}$ and the Doppler width of 79 meV.

Figure 19 presents a portion of the electron spectra of the transitions to the $H_2O^+ X\ 1b_1^{-1}\ ^2B_1$, $A\ 3a_1^{-1}\ ^2A_1$ and $B\ 1b_2^{-1}\ ^2B_2$ states via the $O\ 1s^{-1}2b_2\ (000)$ excited state of H_2O (see figure 16). The upper spectrum is recorded using the gas cell, whereas the lower spectrum is recorded with the molecular beam device. The monochromator bandwidth is $\sim 40\text{ meV}$ and the bandwidth of the electron analyser is $\sim 33\text{ meV}$. The Doppler width due to the thermal motion of the sample molecule at room temperature is $\sim 70\text{ meV}$. One can clearly see the bending vibration $(0, 1, 0)$ at the binding energy of 12.78 eV in the X band only in the ‘Doppler-free’ spectrum. The vibrational structure of the B band is also clearer in the ‘Doppler-free’ spectrum. The most significant difference is, however, seen in the A band, where a long progression of the bending vibrations is clearly seen only in the ‘Doppler-free’ spectrum.

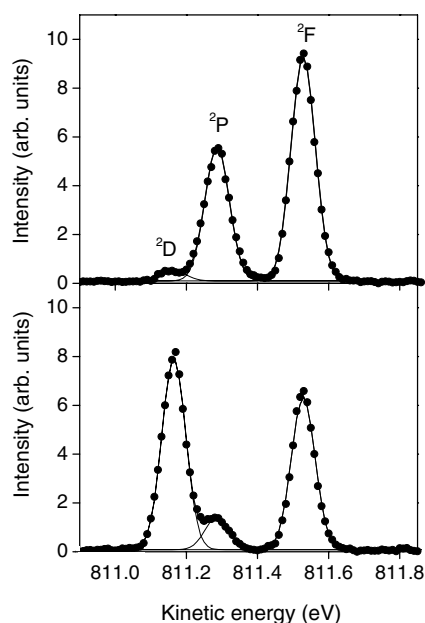


Figure 18. A part of the electron spectra of the resonant Auger transitions of Ne similar to figure 13, but under the ‘Doppler-free’ condition by using the molecular beam device (from [128]).

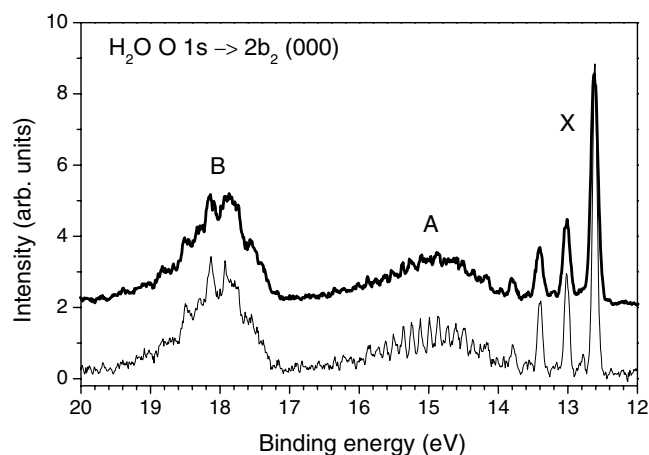


Figure 19. A portion of the resonant photoemission spectra to the $\text{H}_2\text{O}^+ \text{X } 1b_1^{-1} {}^2B_1$, $\text{A } 3a_1^{-1} {}^2A_1$ and $\text{B } 1b_2^{-1} {}^2B_2$ states via the $\text{O } 1s^{-1}2b_2$ excited state. The upper spectrum was recorded with a gas-cell, and the lower one under the ‘Doppler-free’ condition by using the molecular beam device (from [128]).

6. Multiple-ion coincidence momentum imaging

Various types of coincidence technique have been used for investigating molecular dissociation dynamics after inner-shell excitation, as briefly reviewed in section 1. Here we focus on the multiple-ion-coincidence momentum-imaging technique [90, 93].

As seen in section 4.3, the excitation of the C $1s$ inner-shell electron of the CO_2 molecule to $2\pi_u$ leads to the doubly degenerate Π_u state that splits into two Renner–Teller (RT) states

along the bending coordinate Q_2 . The lower branch has a stable bent geometry, whereas the upper branch remains linear. In the following subsections it is shown that the $C\ 1s^{-1}2\pi_u$ RT states can be separated using the multiple-ion-coincidence momentum-imaging technique, and thus the linear and bent geometries can be probed separately [93, 94].

Then we discuss the excitation of the B $1s$ electron of the BF_3 molecule to the lowest unoccupied molecular orbital, $2a_2''$. The ground state BF_3 molecule has a plane triangular geometry that belongs to the D_{3h} point group, whereas the $B\ 1s^{-1}2a_2''$ inner-shell excited state has a trigonometric pyramidal equilibrium geometry with C_{3v} point group [152, 174]. Thus, after the inner-shell excitation, the central B atom is expected to go off transverse to the molecular plane towards the new equilibrium geometry. It is shown that the deformed inner-shell excited BF_3 molecule can be snapshot at the time of the Auger decay by use of the multiple-ion-coincidence momentum-imaging technique [71].

6.1. Probing geometries for Renner–Teller states of CO_2

We consider here the triply charged molecular parent ion CO_2^{3+} produced by the Auger decay of the inner-shell excited states of CO_2 . This triply charged molecular ion has high internal energy and breaks up very rapidly due to the Coulomb explosion. The bond breaking is simultaneous and the axial-recoil approximation [146–148] is valid. Thus, linear momenta of the fragment ions reflect the geometry of the molecule at the time when the Auger decay takes place. The triply charged parent ion CO_2^{3+} may be generated via triple Auger decay and/or very fast sequential decay (of the order of 10^{-15} s). Although the branching ratio for the production of the triply charged molecular parent ion CO_2^{3+} is only a few per cent, it represents well the geometry of the inner-shell excited molecule because the properties of the excited state are independent of decay channels (see figure 8). The bending motion in the A_1 (B_1) state proceeds in the direction parallel (perpendicular) to the electric vector \mathcal{E} of the light. Thus, we can select the A_1 state in which the direction of the bending motion is parallel to \mathcal{E} or the B_1 state in which the molecular plane is perpendicular to \mathcal{E} , by examining the linear momenta of the three fragment ions C^+ , O^+ and O^+ , measured in coincidence by means of the multiple-ion-coincidence momentum-imaging technique.

The vector correlation among the linear momenta of the three fragment ions produced in the three-body break-up $CO_2^{3+} \rightarrow C^+ + O^+ + O^+$ can be well represented by the Newton diagrams. In the Newton diagrams in figure 20 [94], the amplitude of the linear momentum of the first O^+ is normalized to unity and the normalized vector is placed on the negative x axis. The linear momentum of C^+ is then plotted in the positive y direction, and the linear momentum of the second O^+ in the positive x and negative y directions. The intensity is given in the form of contour plots in a linear scale.

Compare diagrams (a) and (b) recorded at the $C\ 1s \rightarrow \sigma^*$ shape resonance at 312 eV and at the $C\ 1s \rightarrow 2\pi_u$ excitation at 290.8 eV, respectively. The C^+ ion goes off slightly transverse to the two O^+ ions on average even at the $C\ 1s \rightarrow \sigma^*$ shape resonance, even though the molecule is believed to have a linear geometry before dissociation. Even though the stable geometry is linear, the C atom goes off slightly transverse to the molecular axis due to zero-point bending vibration. The Coulomb explosion enhances this small displacement, resulting in a non-negligible linear momentum of the C^+ ion transverse to the two O^+ ions. Note also that the Newton diagram is constructed from the measurements for all solid angles. In the procedure of projecting the vector correlation into the reaction plane, one has implicitly introduced the weighting factor of $\sin \theta$, where θ is the correlation angle between the two linear momenta of the two O^+ ions. Thus, one can hardly see the completely linear correlation ($\theta = 180^\circ$) between the two O^+ ions, owing to the weighting factor of $\sin \theta$. At the $C\ 1s \rightarrow 2\pi_u$ excitation,

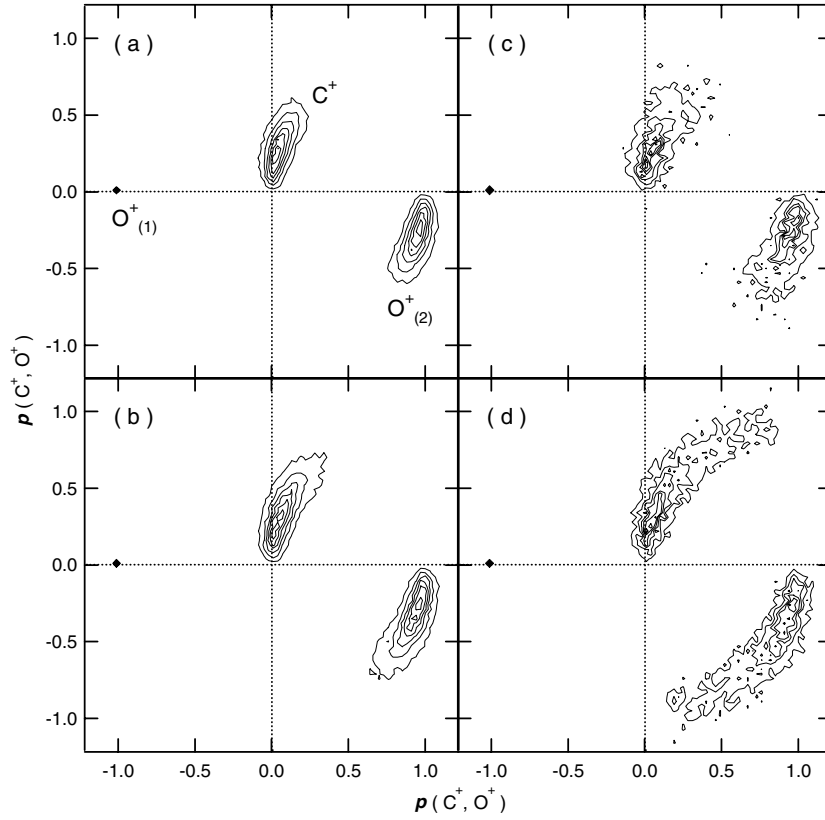


Figure 20. Newton diagrams for the three-body break-up $\text{CO}_2^{3+} \rightarrow \text{C}^+ + \text{O}^+ + \text{O}^+$ (a) for the excitation at the $\text{C } 1s \rightarrow \sigma^*$ shape resonance (312 eV), (b) for the $\text{C } 1s \rightarrow 2\pi_u$ excitation (290.8 eV), (c) for the excitation to the state with the bending motion perpendicular to the electric vector \mathcal{E} (i.e., B_1 in C_{2v}), by 290.8 eV photons, and (d) for the excitation to the state with the bending motion parallel to \mathcal{E} (i.e., A_1 in C_{2v}), by 290.8 eV photons. The scale of the contour plots is linear and relative (from [94]).

one can see the long tail for each island, which illustrates that the C^+ ion goes off transverse to the two O^+ ions more than that at the $\text{C } 1s \rightarrow \sigma^*$ shape resonance.

Compare diagrams (c) and (d). In both diagrams, the excitation energy is set at the $\text{C } 1s \rightarrow 2\pi_u$ excitation peak. In the construction of diagram (c), however, the events are selected in which the vector product of the two linear momenta of the two O^+ ions, $p(\text{O}_{(1)}^+) \times p(\text{O}_{(2)}^+)$, is parallel to \mathcal{E} , with the angles between $p(\text{O}_{(1)}^+) \times p(\text{O}_{(2)}^+)$ and \mathcal{E} smaller than 20° . In this way, the state is selected in which the direction of the bending motion is perpendicular to \mathcal{E} , i.e., the B_1 state in the bent geometry of C_{2v} point group. In constructing diagram (d), on the other hand, the events are selected in which $p(\text{C}^+)$ is parallel to \mathcal{E} , with the angles between $p(\text{C}^+)$ and \mathcal{E} smaller than 20° . In this way, the state is selected in which the direction of the bending motion is parallel to \mathcal{E} , i.e., the A_1 state in the bent geometry of the C_{2v} point group.

Diagram (c) coincides with (a) and illustrates that the displacement of the C atom due to the bending motion does not occur significantly in the direction perpendicular to \mathcal{E} . In other words, the B_1 state thus probed has a linear geometry. In diagram (d), one can clearly see that the very long tail appears for each island, illustrating that the C^+ ion goes off significantly

transverse to the two O^+ ions. This indicates that the bending motion proceeds significantly in the A_1 state. A highly excited bending motion in a linear state with A_1 symmetry, which might cause a tail structure, cannot be excited from the linear ground state due to the Franck–Condon principle. The initial vibrational wavepacket has little momentum. The force to push the C atom at right angles relative to the molecular axis must come, with time evolution, from the electronic potential energy surface. Thus, the state with A_1 symmetry probed here must have a stable bent geometry.

6.2. Probing molecular deformation of inner-shell excited BF_3

The BF_3 molecule has a D_{3h} planar geometry in the ground state, and its electronic configuration is

$$(\text{core})1a_1'^2 1e'^4 2a_1'^2 2e'^4 1a_2''^2 3e'^4 1e''^4 1a_2'^2; 2a_2''^0 4e'^0.$$

Here ‘core’ includes F 1s and B 1s electrons. $1a_1'$ and $1e'$ are inner-valence orbitals whose character is mostly F 2s. The next six occupied orbitals are outer valence orbitals: $2a_1'$, $2e'$ and $1a_2''$ are bonding; $3e'$ and $1e''$ are slightly bonding, having mostly F 2p character, whereas $1a_2'$ is non-bonding, having pure F 2p character. The lowest unoccupied molecular orbital is $2a_2''$, having B $2p_z$ character, and is non-bonding. The $4e'$ unoccupied molecular orbital has antibonding character and in general is located in energy above the ionization threshold, forming a shape resonance.

The B 1s absorption spectrum of BF_3 was investigated by Ishiguro *et al* [175] about 20 years ago. The electronic decay after $B\ 1s \rightarrow 2a_2''$ excitation was investigated by several groups [62, 71, 176–178]. The ionic fragmentation after $B\ 1s \rightarrow 2a_2''$ excitation was investigated by means of various coincidence techniques, such as resonant-Auger-electron-photoion coincidence [86, 88] and photoelectron-photoion-photoion coincidence [174].

Figure 21 presents the total ion spectrum of BF_3 in the B 1s excitation region [71]. The prominent broad band at 195.5 eV corresponds to the promotion of the B 1s electron to the lowest unoccupied molecular orbital, $2a_2''$. The width of this band (FWHM) is ~ 250 meV, much larger than the expected natural lifetime width $\Gamma \sim 60$ meV and the monochromator band width ~ 20 meV. Thus, it is clear that this band consists of unresolved vibrational components whose energy spacings are smaller than the natural lifetime width of the inner-shell hole state. The weak band at 198.2 eV corresponds to the $B\ 1s \rightarrow 3sa_1'$ transition. This transition is electronically forbidden, but it arises as a result of pseudo-Jahn–Teller coupling, that mixes the $B\ 1s^{-1}2a_2''$ and $B\ 1s^{-1}3sa_1'$ states via the out-of-plane ν_2 vibrations of a_2'' symmetry. Vibrational structure is observable in this band. The energy spacing of the two prominent vibrational components is ~ 100 meV, and corresponds to the frequency of the breathing mode ν_1 . The two prominent components are thus assigned to $(\nu_1, 1)$ with $\nu_1 = 0, 1$.

Tanaka *et al* [152] analysed the absorption spectrum for these two bands, $B\ 1s \rightarrow 2a_2''$ and $B\ 1s \rightarrow 3sa_1'$, using the vibronic coupling model. In their analysis, only the ν_2 out-of-plane vibrational mode was taken into account, and the matrix element of the pseudo Jahn–Teller coupling that mixes the $B\ 1s^{-1}2a_2''$ and $B\ 1s^{-1}3sa_1'$ states is estimated in such a way as to reproduce the intensity ratio of these two bands. Because of this coupling, the potential energy curves for the $B\ 1s^{-1}2a_2''$ and $1s^{-1}3sa_1'$ states along the out-of-plane vibrational coordinate Q_2 strongly repel each other near the origin, and thus the $B\ 1s^{-1}2a_2''$ state becomes unstable at the origin. The calculation for the excitation from the ground state to the $B\ 1s^{-1}2a_2''$ state predicted that many unresolved ν_2 vibrational components form a slightly asymmetric band, with a very small tail toward lower energy; one cannot resolve the out-of-plane vibrations, because the vibrational spacings are smaller than the lifetime width. One can however directly probe this

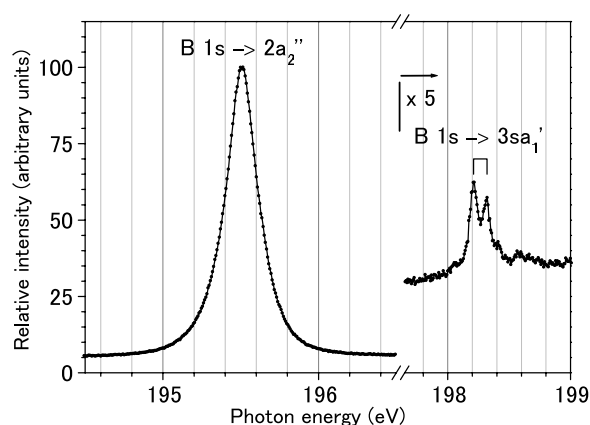


Figure 21. The total ion yield spectrum of BF_3 in the B 1s excitation region (from [71]).

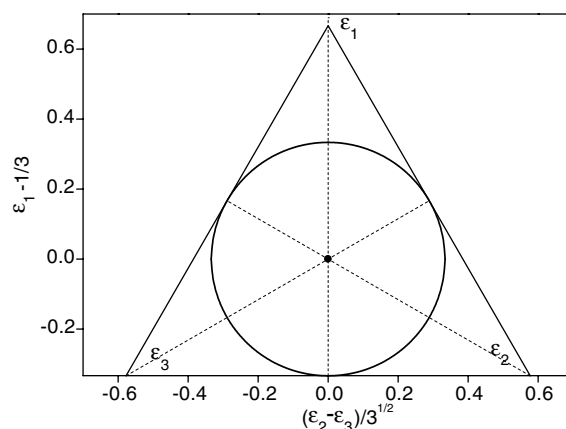


Figure 22. Definition of the Dalitz plot (from [71]); see the text for details.

out-of-plane motion of the central B atom, snap-shooting the deformed molecule at the time of the Auger decay by use of the multiple-ion-coincidence momentum-imaging technique [71].

The quadruply charged BF_3^{4+} molecular parent ion can be produced by the multiple Auger decay of the inner-shell excited or ionized states of BF_3 . This channel is very weak, representing less than 1% of the total ionization yield. This quadruply charged molecular ion has high internal energy and breaks up very rapidly due to Coulomb explosion. Thus, despite the small branching ratio for the formation of the quadruply charged BF_3^{4+} molecular parent ion, the vector correlation among the linear momenta of the four ions reflects the geometry of the inner-shell excited molecule at the time when the Auger decay takes place, because the properties of the excited state are independent of the decay channels.

In the previous subsection we introduced the Newton diagram, in order to represent the vector correlation among the linear momenta of three ions produced by three-body break-up. The alternative way to represent it is the Dalitz plots [180]. Though Dalitz plots may be less familiar than the Newton diagram, they have some advantages in some cases because the three particles are treated equivalently and each point of coordinates has equivalent weight in the

space of Dalitz plots. Figure 22 helps to explain the way to construct the Dalitz plot. We introduce the normalized, squared momentum ϵ_i for each ion i ,

$$\epsilon_i = \frac{|P_i|^2}{\sum_i |P_i|^2}, \quad (25)$$

where P_i is the linear momentum of the ion i , and define the Cartesian coordinates x_D and y_D as

$$x_D = \frac{\epsilon_2 - \epsilon_3}{3^{1/2}}, \quad y_D = \epsilon_1 - \frac{1}{3}. \quad (26)$$

Then all the data points (x, y) are within the circle in figure 22 and the distances from the data point (x, y) to the three sides of the regular triangle are ϵ_i .

In order to use the Dalitz plots for investigating the vector correlation among the four linear momenta of the four particles produced by the four-body break-up, we take the projection of the three linear momenta of the three particles on to the plane perpendicular to the linear momentum of the remaining fourth particle. First, consider the projections of the linear momenta of the three F^+ ions on to the plane perpendicular to the linear momentum of the B^+ ion, i.e., the molecular plane, measured in coincidence. Figure 23 presents the Dalitz plots for the projected linear momenta of the three F^+ ions thus defined. The upper one is recorded at the $B\ 1s \rightarrow 4e'$ shape resonance above the $B\ 1s$ ionization threshold, whereas the lower one is recorded at the $B\ 1s \rightarrow 2a_2''$ excitation. In both cases, most of the events are located near the central part of the Dalitz plots, suggesting that the linear momenta of the three F^+ ions have almost equal sizes and thus the rupture of the three B^+-F^+ bonds is simultaneous and symmetric.

We now investigate the expulsion of the B^+ fragment perpendicular to the molecular plane, in order to obtain evidence for the out-of-plane ν_2 nuclear motion. Let us consider the projections of linear momenta of the B^+ ion and the two F^+ ions on to the plane perpendicular to the linear momentum of the remaining F^+ ion. Figure 24 presents the corresponding Dalitz plots recorded at the $B\ 1s \rightarrow 4e'$ shape resonance and at the $B\ 1s \rightarrow 2a_2''$ excitation. Focus on the data in the upper panel, recorded at the $B\ 1s \rightarrow 4e'$ shape resonance. Most of the data points are close to the bottom. This clearly indicates that the linear momentum of the B^+ ion is small and the ionic dissociation is mainly within the molecular plane. The non-zero component of the B^+ linear momentum is small but still finite. Even though the stable geometry of the $B\ 1s^{-1}4e'$ state and of the $B\ 1s^{-1}$ ionized state is planar, the B atom goes off slightly transverse to the molecular plane, due to the zero-point ν_2 vibration. The Coulomb explosion enhances this small displacement, resulting in a non-negligible component of the linear momentum of the B^+ ion transverse to the molecular plane. Note that the discussion above is parallel to that for $C\ 1s \rightarrow \sigma^*$ excitation, described in the preceding subsection.

Turn your attention to the data in the lower panel, recorded at the $B\ 1s \rightarrow 2a_2''$ excitation. It can be seen that the island at the bottom is elongated towards the positive vertical axis and the intensity in the central part of the Dalitz plot is greatly enhanced, suggesting that the linear momentum of the B^+ ion is increased. Recall that the rupture of the three B^+-F^+ bonds is simultaneous and symmetric, as seen in figure 23. Thus, the increase in the B^+ linear momentum shown in figure 24 is a direct proof that the out-of-plane motion proceeds to a certain extent in the $B\ 1s^{-1}2a_2''$ inner-shell excited state before the Auger decay occurs. Note that the discussion above is parallel to that for $C\ 1s \rightarrow 2\pi_u\ ^1A_1$ excitation described in the preceding subsection.

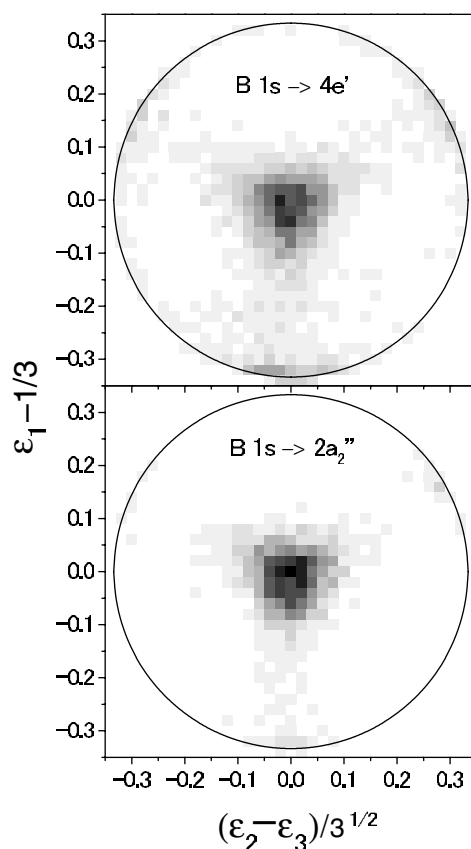


Figure 23. Dalitz plots for the three F^+ fragments produced from BF_3^{4+} . Upper plot, recorded at the $B\ 1s \rightarrow 4e'$ shape resonance. Lower plot, recorded at the $B\ 1s \rightarrow 2a_2''$ excitation. Projections are taken for the linear momenta of the three F^+ ions on to the plane perpendicular to the linear momentum of the B^+ ion, recorded in coincidence (from [71]).

7. Electron-ion coincidence momentum imaging

There have been significant advances in the development of techniques for measuring angular distributions of photoelectrons in the molecular frame (see, for example, [96, 97, 103]). To date, these techniques have been extensively used to study the angular distributions of K-shell photoelectrons emitted from N_2 and CO (see, for example, [96–99, 103–105]). The measurements have confirmed the rich dynamical structure of photoelectron angular distributions in the molecular frame predicted by Dehmer and Dill some 25 years ago [181]. These distributions have been particularly insightful in regions of shape resonances for K-shell photoelectrons from small molecules, where they provide a dynamical window on the underlying partial-wave composition of the photoelectron as it scatters off the anisotropic potential of the ion. Furthermore, recent calculations employing Hartree–Fock and random-phase-approximation methods and an extension of the standard multiple-scattering approach have yielded angular distributions which reproduce key features of the measured spectra quite well [98, 105, 182]. In this section, the extension of this kind of investigation to the triatomic molecule CO_2 is described [106–108]. First, the angular distributions of the C 1s photoelectron in the molecular frame [107, 108] will be discussed. Then, symmetry-

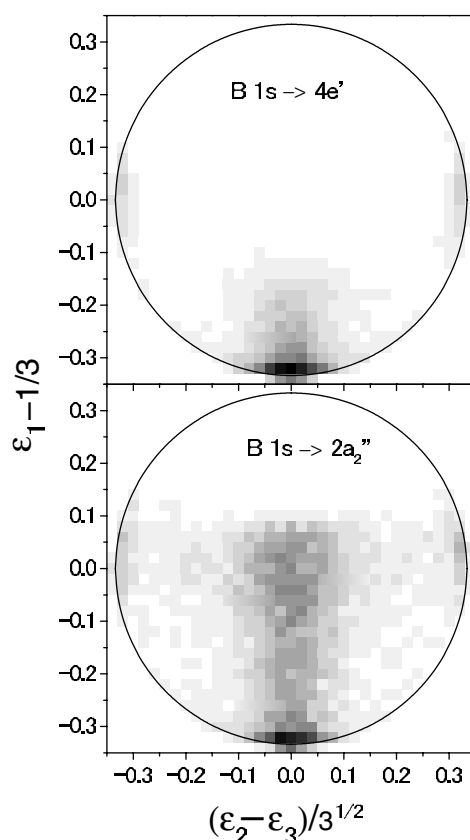


Figure 24. Dalitz plots for the B^+ and two of the three F^+ fragments produced from BF_3^{4+} . Upper plot, recorded at the $B\ 1s \rightarrow 4e'$ shape resonance. Lower plot, recorded at the $B\ 1s \rightarrow 2a_2''$ excitation. Projections are taken for the linear momenta of B^+ and two F^+ onto the plane perpendicular to the linear momentum of the remaining F^+ ion, recorded in coincidence (from [71]).

resolved C 1s photoelectron satellite spectra [106] are presented and discussed as a proof of the breakdown of the conventional shake-up picture.

7.1. Photoelectron angular distributions of CO_2 in the molecular frame

Figure 25 shows the measured (dots) and calculated (lines) angular distributions for photoelectrons emitted from the carbon K shell of fixed-in-space CO_2 at electron kinetic energies of 6.2, 9.4, 14.6, 23.3 and 32.2 eV [107]. The electric vector \mathcal{E} of the light is horizontal and orientations of the molecular axis are 0° , 45° and 90° with respect to \mathcal{E} . The distributions for molecular orientations of 0° and 90° correspond to $\Sigma \rightarrow \Sigma$ (referred to as Σ) and $\Sigma \rightarrow \Pi$ (Π) transitions, respectively. The calculated photoelectron angular distributions were obtained within a relaxed-core Hartree–Fock (RCHF) approximation with a molecular basis set obtained using Slater’s transition state approximation [183]. In this approximation the relaxed molecular orbitals are derived from a self-consistent calculation where half an electron is removed from the carbon K-shell. This procedure attempts to capture effects arising from screening of the K-shell hole while maintaining the calculation at the one-electron level. For better comparison with the measured data, the calculated distributions in figure 25 have been convoluted with a Gaussian distribution with an FWHM of 15° , corresponding to the

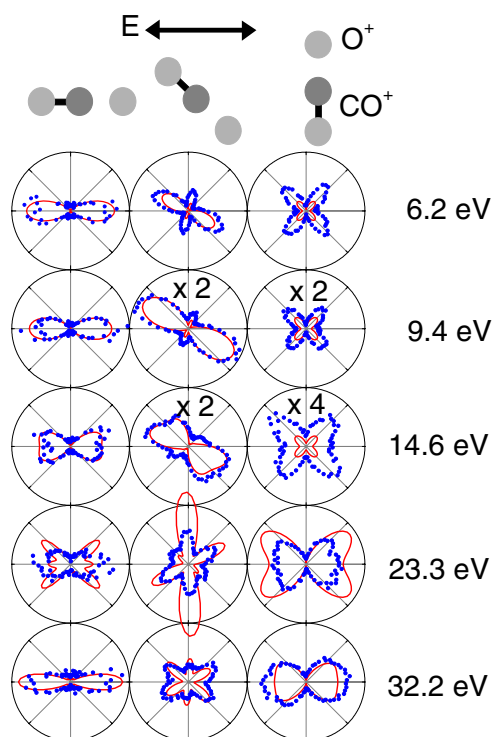


Figure 25. C 1s photoelectron angular distributions from fixed-in-space CO₂ molecules at electron kinetic energies of 6.2, 9.4, 14.6, 23.3 and 32.2 eV. The dots and curves correspond to measurements and calculations, respectively. The direction of electric vector \mathcal{E} is horizontal. The molecular axis is at 0°, 45° and 90° with respect to \mathcal{E} (from [107]).

(This figure is in colour only in the electronic version)

experimental angular resolution. The distribution at each energy is normalized so that the integrated intensity (area enclosed) for the Σ channel is unity, for both the measured and calculated spectra. The distributions for different orientations of the molecular axis (0°, 45° and 90°) are on relative scales. The Σ channel is particularly strong at kinetic energies of 9.4 and 14.6 eV, and thus the corresponding data for 45° and 90° are multiplied by a factor of two or four, as indicated in the figure.

Note that the experiment resolves O⁺ and CO⁺ fragments, and hence the measured photoelectron distributions need not display reflection symmetry through a plane perpendicular to the molecular axis, if the photoemission is related to the asymmetric O⁺–CO⁺ fragmentation. The measured photoelectron distributions do, however, show this symmetry for the Σ and Π channels, and we take this to be an indication that electron emission is independent of asymmetric molecular fragmentation. The calculated photoelectron distributions, which are generally in quantitative agreement with the measured spectra, were obtained in the D_{∞h} point group.

We first discuss the angular distributions in the Σ channel where the electric vector \mathcal{E} is parallel to the molecular axis. In this channel only odd partial wave components of the dipole matrix element arise in photoionization of the C 1s σ_g orbital. The calculated angular distributions in figure 25 reproduce the general features of the measured spectra reasonably well except at an electron energy of 23.3 eV, where the calculated cross section exhibits sharper

structure than may be apparent in the experimental data. The distributions at lower energies of 6.2 and 9.4 eV, ~ 8 and 5 eV below the peak of the shape resonance, respectively, are more peaked along \mathcal{E} than would be expected for the pure p wave. This behaviour very likely arises from interference between the $l = 1$ and 3 waves. At an energy of 14.6 eV in the peak region of the resonance, the angular distribution is not as peaked along the molecular axis as those at lower energies and reflects interference among the $l = 1, 3$ and 5 waves, which are all quite significant around 14 eV. It is worth noting that this behaviour is in sharp contrast with the distribution in the diatomic molecule N_2 where a rich structure dominated by a single $l (= 3)$ is seen.

Agreement between the calculated and measured angular distributions at an electron energy of 23.3 eV in the Σ channel is clearly less satisfactory than at the lower energies in figure 25. The calculated distribution displays sharp structure, which is not apparent in the measured spectra. This disagreement may be due to neglect of vibrational motion in the calculated spectra, which were obtained at the ground state geometry. Finally, the calculated and measured angular distributions at the highest photoelectron energy studied here are quite good.

In the Π channel, where \mathcal{E} is perpendicular to the molecular axis and no shape resonance is seen, the shapes of the calculated and measured angular distributions are in good agreement at the five energies shown in figure 25. The calculated intensities, however, are clearly lower than the measured ones at the lower energies of 6.2, 9.4 and 14.6 eV. This is due to the normalization of the intensities of the calculated and measured distributions in the Σ channel, and an overestimation of the calculated intensities in the shape resonance region of the Σ channel. At lower energies, electron emission along \mathcal{E} is less pronounced than at higher energies and exhibits structure characteristic of an $l = 2$ wave, which is forbidden in this channel. As the energy increases, electron emission along the electric vector becomes more pronounced.

Figure 25 also shows measured and calculated angular distributions for an orientation of 45° between \mathcal{E} and the molecular axis. These distributions are determined by a coherent mixture of the Σ and Π channels, and the ratios of both amplitudes and phases in these channels play a significant role. These distributions can hence be additional benchmarks for testing theoretical methods and models. Agreement between the calculated and measured distributions is quite reasonable, and suggests that the calculated phase relationship between the Σ and Π channels is satisfactory. The underestimation of the intensities of the minor lobes at the lower energies of 6.2 and 9.4 eV is again probably due to an overestimation of the intensity of the Σ channel relative to the Π , as discussed above.

7.2. Symmetry-dependent multielectron excitation of CO_2

The shape resonances are conventionally described as one-electron phenomena, associated either with temporary trapping of the photoelectron by the molecular potential [184] or with the promotion of a core electron to an unoccupied molecular orbital [185]. Recent inner-shell photoemission studies have, however, revealed that multielectron excitations play important roles in the shape resonance regions, raising questions about the validity of one-electron descriptions [186–188]. Such multielectron transitions in molecules have so far mostly been interpreted as results of a shake-up mechanism. Here a core electron absorbs the photon angular momentum. In a dipole transition, it is either emitted to the continuum or to an excited state. The valence electrons are now no longer in an eigenstate of the altered potential, and relax in a monopole transition either to a bound state or to the continuum. The electron emitted to the continuum is then observed either as a normal or conjugate satellite of the main photoline.

From atomic double ionization and ionization with excitation, it is known however that, in addition to shake-up/off, two electron processes can also be induced by an electron–electron

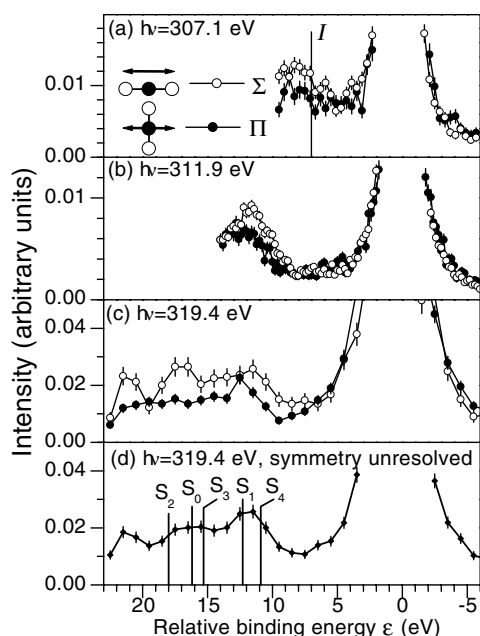


Figure 26. Photoelectron spectra of CO₂ for the molecular axis fixed in space parallel to (Σ), and perpendicular to (Π), the direction of electric vector \mathcal{E} of the light, (a)–(c), and without selection of the molecular axis (d) (from [106]).

scattering (see [189] and references therein). Pavlychev [190] has argued that a similar inelastic scattering of the photoelectron with the valence electrons (i.e., PEVE interaction) could also play a crucial role in multielectron transitions in molecules.

Experimental evidence for the existence of PEVE interaction can be provided by the symmetry-resolved inner-shell photoemission spectra recorded by use of the electron–ion coincidence momentum-imaging technique [106]. The experiment is designed on the basis of the simple idea that

- (i) the probability of normal shake-up/off drops when the photon frequency approaches the ionization threshold [191],
- (ii) the conjugate transitions regarded as monopole valence ionization accompanying the $2\sigma_g \rightarrow 2\pi_u^*$ dipole allowed excitation occur mainly in molecules oriented perpendicular to the direction of the electric vector \mathcal{E} of the light and
- (iii) the photoelectron impact mechanism caused by the PEVE interaction, in contrast, can be expected to have a higher probability for the parallel molecular orientation for which the photoelectron is driven mainly along the molecular axis.

The photoelectron satellite spectra for the Σ and Π transitions, recorded at $h\nu = 307.1$, 311.9 and 319.4 eV, are presented in figure 26 [106]. The spectra are plotted as a function of the satellite state energy, ϵ , relative to the C $1s^{-1}$ ionized state. The uncertainty of this relative energy scale is ~ 1 eV. The intensities of the spectra are normalized to make each integrated intensity equal to unity. The spectrum measured at $h\nu = 319.4$ eV, with no selection made for the molecular axis direction, is also shown, in figure 26(d), for comparison. The relative intensity distribution within each spectrum may be only semiquantitative, since a specific fragmentation channel resulting in two-body dissociation $O^+ + CO^+$ was selected. Even so, the *symmetry-unresolved* spectrum in figure 26(d) shows reasonable agreement with the spectrum

observed by Schmidbauer *et al* [186], at a similar photon energy, at higher resolution, without taking the coincidence with ions, and without selecting the transition symmetry. Schmidbauer *et al* observed five satellite bands, S_0 – S_4 , at energies, ϵ , ranging from 10.9 to 18.0 eV. All these satellite bands are also observed in the spectra recorded at $h\nu = 319.4$ eV (figures 26(c) and (d)). Only S_1 and S_4 can exist at the lower photon energy of 311.9 eV (figure 26(b)), and none of the S_0 – S_4 bands are energetically accessible at 307.1 eV (figure 26(a)). An additional structure, labelled I in figure 26, can also be noticed, at $\epsilon \sim 6$ –8 eV. This I band corresponds to the bands at 5.8 and 7.3 eV observed before [186].

The relative intensity and profile in the symmetry-resolved spectra show significant differences. It is evident that satellites are excited more effectively for the Σ transition. The satellite intensity in the symmetry-unresolved spectrum is intermediate between the Σ - and Π -spectra. Our observation rules out the assignment of the S_3 , S_4 and I bands to the conjugate satellites [186]. According to this assignment, they are expected to be more intense for the Π transitions, which is in contrast to the results in figure 26. The strong enhancement of the satellites for parallel orientation of the molecule provides direct evidence for the photoelectron-impact mechanism: photoelectrons emitted originally along the molecular axis (the Σ transition as seen in figure 25) are much more likely to interact with a valence electron than those which escape perpendicular to the molecule (the Π transition).

8. Concluding remarks

We looked at beamlines and endstations devoted to atomic and molecular science at the third-generation SR facilities as well as the research activities on inner-shell spectroscopies. Then we focused on the soft-x-ray photochemistry beamline at SPring-8 and looked into the details of the endstations and research activities on inner-shell spectroscopies of Ne, H₂O, CO₂ and BF₃. Although the subjects described here are very limited, we can still see the general trends of inner-shell spectroscopies of free atoms and molecules using the third-generation SR sources.

Third-generation SR sources and high-resolution soft-x-ray monochromators are widely used for photoabsorption and ion yield spectroscopies as well as inner-shell photoelectron spectroscopy, in order to disentangle vibronic structures in the inner-shell excited or ionized states of molecules. Ion yield measurements of H₂O and CO₂ described here are typical examples of such investigations. Especially, the CO₂ molecule, discussed in detail here, is a typical prototype molecule suitable for studying vibronic interactions that cause symmetry breaking and molecular deformation. Vibronic interactions and molecular deformations of more complex larger molecules, such as benzene, furane, fullerenes etc, are under investigation at some third-generation SR facilities. Spin–orbit and exchange interactions, as well as molecular-field-splitting effects, not discussed here but important for excitations and ionizations of 2p, 3d etc, are also under investigation, using ion yield spectroscopy and photoelectron spectroscopy.

A combination of a third-generation SR source, a high-resolution soft-x-ray monochromator and a high-resolution electron spectrometer is nowadays essential to perform molecular resonant photoemission spectroscopy, in order to investigate the relevant potential energy surfaces and nuclear motions along these surfaces. Resonant photoemission study of H₂O described here is a typical example of such investigations. Furthermore, this combination invokes investigations of weak but very informative processes that have not been fully investigated, such as photoemission via excitation in the inter-resonance regions, via multiply excited states etc. The photoemission study of Ne described here is a typical example of such investigations. Investigations of decay processes of multiply excited states are also in progress. Resonant photoemission studies on open-shell molecules and radicals and heavy-

atom-containing molecules, not discussed here, are also in progress at some third-generation SR facilities.

In coincidence experiments, it is generally considered that a large photon flux is unfavoured, because signal to noise ratios are proportional to the square of coincidence rates. This may be a reason why coincidence techniques are not used extensively with the third-generation SR sources, where a large photon flux from the undulator is available. Multi-coincidence momentum-imaging techniques described here can fully benefit from a large photon flux, because the detection angles for each particle are 4π sr, and thus false coincidence rates are very low. Experiments described here are typical examples and various extensions are possible. Note that one can fix a bent triatomic molecule and a C_{3v} molecule in space using the triple-ion and quadruple-ion coincidence momentum-imaging techniques. Thus, it is straightforward to extend the electron-ion coincidence momentum-imaging technique to such molecules, in order to investigate inner-shell photoelectron angular distributions in the molecular frame. Such investigations are also in progress.

Acknowledgments

The experiments described here as examples were carried out with the approval of the SPring-8 programme advisory committee. The author is grateful to collaborators listed as authors of [15–18, 35, 48, 68, 71, 93, 94, 106–108, 128] for invaluable contributions to a series of research projects and helpful discussion. The author acknowledges financial support by the Japan Society of the Promotion of Science in the form of Grants-in-Aid for Scientific Research and further support by the Matsuo Foundation.

References

- [1] Prince K C, Vondráček M, Karvonen J, Coreno M, Camilloni R, Avaldi L and de Simone M 1999 *J. Electron Spectrosc. Relat. Phenom.* **101–103** 141
- [2] Coreno M, Avaldi L, Camilloni R, Prince K C, de Simone M, Karvonen J, Colle R and Simonucci M 1999 *Phys. Rev. A* **59** 2494
- [3] Coreno M, de Simone M, Prince K C, Richter R, Vondráček M, Avaldi L and Camilloni R 1999 *Chem. Phys. Lett.* **306** 269
- [4] Prince K C, Avaldi L, Coreno M, Camilloni R and de Simone M 1999 *J. Phys. B: At. Mol. Opt. Phys.* **32** 2551
- [5] de Simone M, Coreno M, Alagia M, Richter R and Prince K C 2002 *J. Phys. B: At. Mol. Opt. Phys.* **35** 61
- [6] Nenner I and Morin P 1996 *VUV and Soft X-Ray Photoionization* ed U Becker and D Shirley (New York: Plenum) p 291
- [7] Hitchcock A P and Neville J J 2002 *Chemical Applications of Synchrotron Radiation* ed T-K Sham (Singapore: World Scientific) p 154
- [8] Shigemasa E, Ueda K, Sato Y, Sasaki T and Yagishita A 1992 *Phys. Rev. A* **45** 2915
- [9] Yagishita A, Shigemasa E, Adachi J and Kosugi N 1993 *Proc. 10th Int. Conf. on Vacuum Ultraviolet Radiation Physics* ed F J Willeumier, Y Petroff and I Nenner (Singapore: World Scientific) p 201
- [10] Kosugi N 2002 *Chemical Applications of Synchrotron Radiation* ed T-K Sham (Singapore: World Scientific) p 228
- [11] Stolte W C, Hansen D L, Piancastelli M N, Domigues Lopez I, Rizvi A, Hemmers O, Wang H, Schlachter A S, Lubell M S and Lindle D W 2001 *Phys. Rev. Lett.* **86** 4504
- [12] Stranges S, Alagia M, Fronzoni G and Decleva P 2001 *J. Phys. Chem. A* **105** 3400
- [13] Stranges S, Richter R and Alagia M 2002 *J. Chem. Phys.* **116** 3676
- [14] Saito N *et al* 2000 *Phys. Rev. A* **62** 042503
- [15] Okada K *et al* 2000 *Chem. Phys. Lett.* **326** 314
- [16] Hiraya A *et al* 2001 *Phys. Rev. A* **63** 042705
- [17] Yoshida H, Nobusada K, Okada K, Tanimoto S, Saito N, De Fanis A and Ueda K 2002 *Phys. Rev. Lett.* **88** 083001
- [18] Okada K, Yoshida H, Senba Y, Kamimori K, Tamenori Y, Ohashi H, Ueda K and Ibuki T 2002 *Phys. Rev. A* **66** 032503

- [19] Carroll T X, Berrah N, Bozek J, Hahne J, Kukk E, Sæthre L J and Thomas T D 1999 *Phys. Rev. A* **59** 3386
- [20] Carroll T X, Hahne J, Thomas T D, Sæthre L J, Berrah N, Bozek J and Kukk E 2000 *Phys. Rev. A* **61** 042503
- [21] Jurvansuu M, Kivimäki A and Aksela S 2001 *Phys. Rev. A* **64** 012502
- [22] Børve K J, Sæthre L J, Thomas T D, Carroll T X, Berrah N, Bozek J D and Kukk E 2001 *Phys. Rev. A* **63** 012506
- [23] Karlsen T, Sæthre L J, Børve K J, Berrah N, Kukk E, Bozek J D, Carroll T X and Thomas T D 2001 *J. Phys. Chem. A* **105** 7700
- [24] Hergenbahn U, Kugeler O, Rennie E E, Rüdel A and Marburger S 2002 *Surf. Rev. Lett.* **9** 13
- [25] Wang H, Snell G, Hemmers O, Sant'Anna M M, Sellin I, Berrah N, Lindle D W, Deshmukh P C, Haque N and Manson S T 2001 *Phys. Rev. Lett.* **87** 123004
- [26] Kukk E, Bozek J D, Sheehy J A, Langhoff P W and Berrah N 2000 *J. Phys. B: At. Mol. Opt. Phys.* **33** L51
- [27] Thomas T D, Berrah N, Bozek J, Carroll T X, Hahne J, Karlsen T, Kukk E and Sæthre L J 1999 *Phys. Rev. Lett.* **82** 1120
- [28] Hergenbahn U, Kugeler O, Rüdel A, Rennie E and Bradshaw A M 2001 *J. Phys. Chem. A* **105** 5704
- [29] Lindle D W and Hemmers O 1999 *J. Electron Spectrosc. Relat. Phenom.* **100** 297
- [30] Hemmers O, Wang H, Focke P, Sellin I A, Lindle D W, Arce J C, Sheehy J A and Langhoff P W 2001 *Phys. Rev. Lett.* **87** 273003
- [31] Püttner R, Pennanen V, Matila T, Kivimäki A, Jurvansuu M, Aksela H and Aksela S 2002 *Phys. Rev. A* **65** 042505
- [32] Kivimäki A, Naves de Brito A, Aksela S, Aksela H, Sairanen O-P, Ausmees A, Osborne S J, Dantas L B and Svensson S 1993 *Phys. Rev. Lett.* **71** 4307
- [33] Åberg T and Crasemann B 1994 *Resonant Anomalous X-Ray Scattering* ed G Materlik, C J Sparks and K Fischer (Amsterdam: North-Holland)
- [34] Armen G B, Aksela H, Åberg T and Aksela S 2000 *J. Phys. B: At. Mol. Opt. Phys.* **33** R49
- [35] Shimizu Y *et al* 2000 *J. Phys. B: At. Mol. Opt. Phys.* **33** L685
- [36] Huttula S-M, Heinäsmäki S, Aksela H, Tulkki J, Kivimäki A, Jurvansuu M and Aksela S 2001 *Phys. Rev. A* **63** 032703
- [37] Sankari R, Kivimäki A, Huttula M, Aksela H, Aksela S, Coreno M, Turri G, Camilloni R, de Simone M and Prince K C 2001 *Phys. Rev. A* **63** 032715
- [38] Kivimäki A, Heinäsmäki S, Jurvansuu M, Alitalo S, Nömmiste E, Aksela H and Aksela S 2001 *J. Electron Spectrosc. Relat. Phenom.* **114–116** 49
- [39] Snell G, Martins M, Kukk E, Cheng W T and Berrah N 2001 *Phys. Rev. A* **63** 062715
- [40] De Fanis A, Saito N, Kitajima M, Shimizu Y, Okada K, Tanaka H, Koyayo I and Ueda K 2001 *J. Phys. B: At. Mol. Opt. Phys.* **34** L377
- [41] De Fanis A, Ueda K, Saito N, Kitajima M, Tanaka H, Shimizu Y, Okada K and Koyayo I 2002 *Surf. Rev. Lett.* **9** 51
- [42] Camilloni R, Žitnik M, Comicioli C, Prince K C, Zacchigna M, Crotti C, Ottaviani C, Quaresima C, Perfetti P and Stefani G 1996 *Phys. Rev. Lett.* **77** 2646
- [43] Canton-Rogan S E, Wills A A, Gorczyca T W, Wiedenhoeft M, Nayandin O, Liu C-N and Berrah N 2000 *Phys. Rev. Lett.* **85** 3113
- [44] Marinho R R T, Björneholm O, Sorensen S L, Hjelte I, Sundin S, Bässler M, Svensson S and Naves de Brito A 2001 *Phys. Rev. A* **63** 032514
- [45] Nayandin O, Gorczyca T W, Wills A A, Langer B, Bozek J D and Berrah N 2001 *Phys. Rev. A* **64** 022505
- [46] Sankari R *et al* 2002 *Phys. Rev. A* **65** 042702
- [47] Saito N, Kabachnik N M, Shimizu Y, Yoshida H, Ohashi H, Tamenori Y, Suzuki I H and Ueda K 2000 *J. Phys. B: At. Mol. Opt. Phys.* **33** L729
- [48] De Fanis A, Saito N, Yoshida H, Senba Y, Tamenori Y, Ohashi H, Tanaka H and Ueda K 2002 *Phys. Rev. Lett.* **89** 243001
- [49] Piancastelli M N 2000 *J. Electron Spectrosc. Relat. Phenom.* **107** 1
- [50] Kukk E, Bozek J D, Cheng W-T, Fink R F, Wills A A and Berrah N 1999 *J. Chem. Phys.* **111** 9642
- [51] Kukk E, Bozek J D and Berrah N 2000 *Phys. Rev. A* **62** 032708
- [52] Kukk E, Snell G, Bozek J D, Cheng W-T and Berrah N 2001 *Phys. Rev. A* **63** 062702
- [53] Björneholm O *et al* 2000 *Phys. Rev. Lett.* **84** 2826
- [54] Piancastelli M N *et al* 2000 *J. Phys. B: At. Mol. Opt. Phys.* **33** 1819
- [55] Feifel R *et al* 2000 *Phys. Rev. Lett.* **85** 3133
- [56] Hjelte I *et al* 2001 *Chem. Phys. Lett.* **334** 151
- [57] Sorensen S L, Fink R F, Feifel R, Piancastelli M N, Bässler M, Miron C, Wang H, Hjelte I, Björneholm O and Svensson S 2001 *Phys. Rev. A* **64** 012719

- [58] Miron C *et al* 2001 *J. Chem. Phys.* **115** 864
- [59] Rosenqvist L *et al* 2001 *J. Chem. Phys.* **115** 3614
- [60] Naves de Brito A, Hjelte I, Wiesner K, Feifel R, Bässler M, Sorensen S L, Björneholm O, Piancastelli M N, Karlsson L and Svensson S 2001 *Phys. Rev. A* **64** 054702
- [61] Fink R F *et al* 2002 *Phys. Rev. A* **65** 034705
- [62] Miron C, Feifel R, Björneholm O, Svensson S, Naves de Brito A, Sorensen S L, Piancastelli M N, Simon M and Morin P 2002 *Chem. Phys. Lett.* **359** 48
- [63] Feifel R, Karlsson L, Piancastelli M N, Fink R F, Bässler M, Björneholm O, Wiesner K, Miron C, Wang H, Giertz A, Sorensen S L, Naves de Brito A and Svensson S 2002 *Phys. Rev. A* **65** 052701
- [64] Feifel R, Gel'mukhanov F, Baev A, Ågren H, Piancastelli M N, Bässler M, Miron C, Sorensen S L, Naves de Brito A, Björneholm O, Karlsson L and Svensson S 2002 *Phys. Rev. Lett.* **89** 103002
- [65] Wiesner K, Naves de Brito A, Sorensen S L, Burmeister F, Gisselbrecht M, Svensson S and Björneholm O 2002 *Chem. Phys. Lett.* **354** 382
- [66] Piancastelli M N *et al* 2002 *Phys. Rev. Lett.* **88** 243002
- [67] Muramatsu Y, Shimizu Y, Yoshida H, Okada K, Saito N, Koyano I, Tanaka H and Ueda K 2000 *Chem. Phys. Lett.* **330** 91
- [68] De Fanis A *et al* 2002 *J. Phys. B: At. Mol. Opt. Phys.* **35** L23
- [69] Baev A, Gel'mukhanov F, Salek P, Ågren H, Ueda K, De Fanis A, Okada K and Sorensen S 2002 *Phys. Rev. A* **66** 022509
- [70] Ueda K 2002 *Surf. Rev. Lett.* **9** 21
- [71] Ueda K *et al* 2003 *Chem. Phys.* at press
- [72] Von Raven E, Meyer M, Pahler M and Sonntag B 1990 *J. Electron Spectrosc. Relat. Phenom.* **52** 677
- [73] Kämmerling B and Schmidt V 1991 *Phys. Rev. Lett.* **67** 1848
- [74] Becker U 1998 *J. Electron Spectrosc. Relat. Phenom.* **96** 105
- [75] Ueda K, Shimizu Y, Chiba H, Sato Y, Kitajima M, Tanaka H and Kabachnik N M 1999 *Phys. Rev. Lett.* **83** 5463
- [76] Wehlitz R, Pibida L S, Levin J C and Sellin I A 1999 *Phys. Rev. A* **59** 421
- [77] De Fanis A, West J B, Ross K J, Ueda K, Beyer H-J, Amusia M Ya and Chernysheva L V 1999 *J. Phys. B: At. Mol. Opt. Phys.* **32** 5739
- [78] Lablanquie P, Penent F, Hall R I, Kjedsen H, Eland J H D, Muehleisen A, Pelicon P, Šmit Ž, Žitník M and Koike F 2000 *Phys. Rev. Lett.* **84** 47
- [79] Eberhardt W, Berstorff S, Jochims H W, Whitfield S B and Crasemann B 1988 *Phys. Rev. A* **38** 3808
- [80] Levin J C, Biedermann C, Keller N, Liljeby L, O C-S, Short R T, Sellin I A and Lindle D W 1990 *Phys. Rev. Lett.* **65** 988
- [81] Kämmerling B, Krässig B and Schmidt V 1992 *J. Phys. B: At. Mol. Opt. Phys.* **25** 3621
- [82] Turri G, Battera G, Avaldi L, Camilloni R, Coreno M, Ruocco A, Colle R, Simonucci S and Stefani G 2001 *J. Electron Spectrosc. Relat. Phenom.* **114–116** 199
- [83] Ricz S, Kövér Á, Juvansuu M, Varga D, Molnár J and Aksela S 2002 *Phys. Rev. A* **65** 042707
- [84] Tamenori Y *et al* 2002 *J. Phys. B: At. Mol. Opt. Phys.* **35** 2799
- [85] Eberhardt W, Sham T K, Carr R, Krummacker S, Strongin M, Weng S L and Wesner D 1983 *Phys. Rev. Lett.* **50** 1038
- [86] Ueda K, Chiba H, Sato Y, Hayaishi T, Shigemasa E and Yagishita A 1992 *Phys. Rev. A* **46** R5
- [87] Lebrun T, Lavollée M, Simon M and Morin P 1993 *J. Chem. Phys.* **98** 2534
- [88] Ueda K, Ohmori K, Okunishi M, Chiba H, Shimizu Y, Sato Y, Hayaishi T, Shigemasa E and Yagishita A 1995 *Phys. Rev. A* **52** R1815
- [89] Miron C, Simon M, Leclercq N, Hansen D L and Morin P 1998 *Phys. Rev. Lett.* **81** 4104
- [90] Lavollée M and Brems V 1999 *J. Chem. Phys.* **110** 918
- [91] Ueda K, Simon M, Miron C, Leclercq N, Guillemin R, Morin P and Tanaka S 1999 *Phys. Rev. Lett.* **83** 3800
- [92] Morin P, Simon M, Miron C, Leclercq N, Kuk E, Bozek J D and Berrah N 2000 *Phys. Rev. A* **61** 050701
- [93] Muramatsu Y *et al* 2002 *Phys. Rev. Lett.* **88** 133002
- [94] Muramatsu Y *et al* 2002 *Surf. Rev. Lett.* **9** 93
- [95] Kuk E, Rius i Riu J, Stankiewicz M, Hatherly P A, Erman P, Rachlew E, Winiarczyk P, Huttula M and Aksela S 2002 *Phys. Rev. A* **66** 012704
- [96] Shigemasa E, Adachi J, Oura M and Yagishita A 1995 *Phys. Rev. Lett.* **74** 359
- [97] Heiser F, Geßner G, Viefhaus J, Wieliczek K, Hentges R and Becker U 1997 *Phys. Rev. Lett.* **79** 2435
- [98] Cherepkov N A, Semenov S K, Hikosaka Y, Ito K, Motoki S and Yagishita A 2000 *Phys. Rev. Lett.* **84** 250
- [99] Motoki S, Adachi J, Hikosaka Y, Ito K, Sano M, Soejima K, Yagishita A, Raseev G and Cherepkov N A 2000 *J. Phys. B: At. Mol. Opt. Phys.* **33** 4193

- [100] Golovin A V, Cherepkov N A and Kuznetsov V V 1992 *Z. Phys. D* **24** 371
- [101] Guillemin R, Shigemasa E, Le Guen K, Ceolin D, Miron C, Leclercq N, Ueda K, Morin P and Simon M 2000 *Rev. Sci. Instrum.* **71** 4387
- [102] Guillemin R, Shigemasa E, Le Guen K, Ceolin D, Miron C, Leclercq N, Morin P and Simon M 2001 *Phys. Rev. Lett.* **87** 203001
- [103] Landers A *et al* 2001 *Phys. Rev. Lett.* **87** 013002
- [104] Weber Th *et al* 2001 *J. Phys. B: At. Mol. Opt. Phys.* **34** 3669
- [105] Jahnke T *et al* 2002 *Phys. Rev. Lett.* **88** 073002
- [106] De Fanis A *et al* 2002 *Phys. Rev. Lett.* **89** 023006
- [107] Saito N *et al* 2003 *J. Phys. B: At. Mol. Opt. Phys.* **36** L25
- [108] Saito N, Ueda K and Koyano I 2003 *Proc. 19th Int. Conf. on X-Ray and Inner-Shell Processes (AIP Proc.)* vol 652, ed A Bianconi, A Marcelli and N L Saini (New York: American Institute of Physics) p 172
- [109] Berrah N, Langer B, Wills A A, Kukk E, Bozek J D, Farhat A and Gorczyca T W 1999 *J. Electron Spectrosc. Relat. Phenom.* **101–103** 1
- [110] Snell G, Vieffhaus J, Dunning F B and Berrah N 2000 *Rev. Sci. Instrum.* **71** 2608
- [111] Snell G, Langer B, Young A T and Berrah N 2002 *Phys. Rev. A* **66** 022701
- [112] Covington A M *et al* 2001 *Phys. Rev. Lett.* **87** 243002
- [113] Berrah N *et al* 2001 *Phys. Rev. Lett.* **87** 253002
- [114] Berrah N, Bozek J D, Turri G, Akerman G, Rude B, Zhou H-L and Manson S T 2002 *Phys. Rev. Lett.* **88** 093001
- [115] Prince K C *et al* 1998 *J. Synchrotron Radiat.* **5** 565
- [116] Blyth R R *et al* 1999 *J. Electron Spectrosc. Relat. Phenom.* **101–103** 959
- [117] Bässler M *et al* 1999 *J. Electron Spectrosc. Relat. Phenom.* **101–103** 953
- [118] Bässler M *et al* 2001 *Nucl. Instrum. Methods A* **469** 382
- [119] Ohashi H, Ishiguro E, Tamenori Y, Kishimoto H, Tanaka M, Irie M, Tanaka T and Ishikawa T 2001 *Nucl. Instrum. Methods A* **467/468** 529
- [120] Tanaka T and Kitamura H 1995 *Nucl. Instrum. Methods A* **364** 368
- [121] Tanaka T and Kitamura H 1996 *J. Synchrotron Radiat.* **3** 47
- [122] Hettrick M C and Bowyer S 1983 *Appl. Opt.* **22** 3921
- [123] Ishiguro E, Ohashi H, Lu L, Watari W, Kamizato M and Ishikawa T 1999 *J. Electron Spectrosc. Relat. Phenom.* **101–103** 979
- [124] Ohashi H *et al* 2001 *Nucl. Instrum. Methods A* **467/468** 533
- [125] Koyano I, Okuyama M, Ishiguro E, Hiraya A, Ohashi H, Kanashima T, Ueda K, Suzuki I H and Ibuki T 1998 *J. Synchrotron Radiat.* **5** 545
- [126] Ueda K *et al* 2001 *Nucl. Instrum. Methods A* **467/468** 1502
- [127] Yoshida H *et al* 2000 *J. Phys. B: At. Mol. Opt. Phys.* **33** 4343
- [128] Tamenori *et al* 2003 *Proc. 19th Int. Conf. on X-Ray and Inner-Shell Processes (AIP Proc.)* vol 652, ed A Bianconi, A Marcelli and N L Saini (New York: American Institute of Physics) p 71
- [129] Shimizu Y *et al* 2001 *J. Electron Spectrosc. Relat. Phenom.* **114–116** 63
- [130] Wiley W C and McLaren I H 1955 *Rev. Sci. Instrum.* **26** 1150
- [131] See <http://roentdek.com> for details on the detectors
- [132] Chen C T, Ma Y and Sette F 1989 *Phys. Rev. A* **40** 6737
- [133] Gadea F X, Köppel H, Schirmer J, Cederbaum L S, Randall K J, Bradshaw A M, Ma Y, Sette F and Chen C T 1991 *Phys. Rev. Lett.* **66** 883
- [134] Remmers G, Domke M and Kaindl G 1993 *Phys. Rev. A* **47** 3085
- [135] Schirmer J, Trofimov A B, Randall K J, Feldhaus J, Bradshaw A M, Ma Y, Chen C T and Sette F 1993 *Phys. Rev. A* **47** 1136
- [136] Breinig M, Chen M H, Ice G E, Parente F, Crasemann B and Brown G S 1980 *Phys. Rev. A* **22** 520
- [137] Fano U and Cooper J W 1968 *Rev. Mod. Phys.* **40** 441
- [138] Fano U 1961 *Phys. Rev.* **124** 1866
- [139] Kuchitsu K 1998 *Structure of Free Polyatomic Molecules—Basic Data* (Berlin: Springer) p 58
- [140] Herzberg G 1966 *Molecular Spectra and Molecular Structure Electronic vol 3 Spectra and Electronic Structure of Polyatomic Molecules* (New York: Van Nostrand) p 402
- [141] Piancastelli M N, Hempelmann A, Heiser F, Geßner O, Rüdell A and Becker U 1999 *Phys. Rev. A* **59** 300
- [142] Cesar A, Ågren H and Carravetta V 1989 *Phys. Rev. A* **40** 187
- [143] Saito N and Suzuki I H 1988 *Phys. Rev. Lett.* **61** 2740
- [144] Yagishita A, Maezawa H, Ukai M and Shigemasa E 1989 *Phys. Rev. Lett.* **62** 36
- [145] Lee K, Kim D Y, Ma C I, Lapiano-Smith D A and Hanson D M 1990 *J. Chem. Phys.* **93** 7936

- [146] Zare R N 1972 *Mol. Photochem.* **4** 1
- [147] Busch G E and Wilson K R 1972 *J. Chem. Phys.* **56** 3638
- [148] Dehmer J L and Dill D 1978 *Phys. Rev. A* **18** 164
- [149] Kim D Y, Lee K, Ma C I, Mahalingam M, Hanson D M and Hulbert S L 1992 *J. Chem. Phys.* **97** 5915
- [150] Domcke W and Cederbaum L S 1977 *Chem. Phys.* **25** 189
- [151] Köppel H, Domcke W and Cederbaum L S 1984 *Adv. Chem. Phys.* **57** 59
- [152] Tanaka S, Kayanuma Y and Ueda K 1998 *Phys. Rev. A* **57** 3437
- [153] Ueda K, Tanaka S, Shimizu Y, Muramatsu Y, Chiba H, Hayaishi T, Kitajima M and Tanaka H 2000 *Phys. Rev. Lett.* **85** 3129
- [154] Kivimäki A, Kempgens B, Maier K, Köppe H, Piancastelli M N, Neeb M and Bradshaw A M 1997 *Phys. Rev. Lett.* **79** 998
- [155] Dobrodey N V, Köppel H and Cederbaum L S 1999 *Phys. Rev. A* **60** 1988
- [156] Cederbaum L S 1995 *J. Chem. Phys.* **103** 562
- [157] Cesar A, Gel'mukhanov F, Luo Y, Ågren H, Skytt P, Glans P, Guo J, Gunnelin K and Nordgren J 1997 *J. Chem. Phys.* **106** 3439
- [158] Malinovskaya S A and Cederbaum L S 2000 *Phys. Rev. A* **61** 042706
- [159] Herzberg G 1973 *Infrared and Raman Spectra of Polyatomic Molecules* (New York: Van Nostrand)
- [160] Wight G R and Brion C E 1974 *J. Electron Spectrosc. Relat. Phenom.* **3** 191
- [161] Adachi J, Kosugi N, Shigemasa E and Yagishita A 1997 *J. Chem. Phys.* **107** 4919
- [162] Niu A F, Zhang Y, Zhang W H and Li J M 1998 *Phys. Rev. A* **57** 1912
- [163] Jolly W L, Bomben K D and Eyermann C J 1984 *At. Data Nucl. Data Tables* **31** 433
- [164] Adachi J, Takata Y, Shigemasa E, Kosugi N and Yagishita A 1999 *Photon Factory Activity Rep.* **16** 9
- [165] Cederbaum L S and Domcke W 1976 *J. Chem. Phys.* **64** 603
- [166] Domcke W and Cederbaum L S 1976 *J. Chem. Phys.* **64** 612
- [167] Osborne S J *et al* 1997 *J. Chem. Phys.* **106** 1661
- [168] Sæthre L J, Sværen O, Svensson S, Osborne S, Thomas T D, Jauhiainen J and Aksela S 1997 *Phys. Rev. A* **55** 2748
- [169] Rubensson J-E, Neeb M, Bringer A, Biermann M and Eberhardt W 1996 *Chem. Phys. Lett.* **257** 447
- [170] Kabachnik N M and Sazhina I P 1976 *J. Phys. B: At. Mol. Phys.* **9** 1681
- [171] Starace A F 1977 *Phys. Rev. A* **16** 231
- [172] Reutt J E, Wang L S, Lee Y T and Shirley D A 1986 *J. Chem. Phys.* **85** 6928
- [173] Gel'mukhanov F K, Mazalov L N and Kondratenko A V 1977 *Chem. Phys. Lett.* **46** 133
- Kaspar F, Domcke W and Cederbaum L S 1979 *Chem. Phys.* **44** 33
- [174] Simon M, Morin P, Lablanquie P, Lavollée M, Ueda K and Kosugi N 1995 *Chem. Phys. Lett.* **238** 42
- [175] Ishiguro E, Iwata S, Suzuki T, Mikuni A and Sasaki T 1982 *J. Phys. B: At. Mol. Phys.* **15** 1841
- [176] Kanamori H, Iwata S, Mikuni A and Sasaki T 1984 *J. Phys. B: At. Mol. Phys.* **17** 3887
- [177] Ueda K, Chiba H, Sato Y, Hayaishi T, Shigemasa E and Yagishita A 1994 *J. Chem. Phys.* **101** 3520
- [178] Simon M, Miron C, Leclercq N, Morin P, Ueda K, Sato Y, Tanaka S and Kayanuma Y 1997 *Phys. Rev. Lett.* **79** 3857
- [179] Shimizu Y, Ueda K, Chiba H, Okunishi M, Ohmori K, West J B, Sato Y and Hayaishi T 1997 *J. Chem. Phys.* **107** 2419
- [180] Dalitz R H 1953 *Phil. Mag.* **44** 1068
- [181] Dehmer J L and Dill D 1975 *Phys. Rev. Lett.* **35** 213
- [182] Cherepkov N A, Raseev G, Adachi J, Hikosaka Y, Ito K, Motoki S, Sano M, Soejima K and Yagishita A 2000 *J. Phys. B: At. Mol. Opt. Phys.* **33** 4213
- [183] Slater J C 1974 *The Self-Consistent Field for Molecules and Solids: Quantum Theory of Molecules and Solids* vol 4 (New York: McGraw-Hill)
- [184] Dehmer J L, Dill D and Parr A C 1985 *Photophysics and Photochemistry in the Vacuum Ultraviolet* ed S McGlynn, G Findly and R Huebner (Dordrecht: Reidel) p 341
- [185] Gianturco F A, Guidotti M and Lamanna U 1972 *J. Chem. Phys.* **57** 840
- [186] Schmidbauer M A, Kilcoyne A L D, Köppe H M, Feldhaus J and Bradshaw A M 1995 *Phys. Rev. A* **52** 2095
- [187] Maier K, Kivimäki A, Kempgens B, Hegenhahn U, Neeb M, Rüdell A, Piancastelli M N and Bradshaw A M 1998 *Phys. Rev. A* **58** 3654
- [188] Piancastelli M N 1999 *J. Electron Spectrosc. Relat. Phenom.* **100** 167
- [189] Kheifets A 2001 *J. Phys. B: At. Mol. Opt. Phys.* **34** L247
- [190] Pavlychev A A 1999 *J. Phys. B: At. Mol. Opt. Phys.* **32** 2077
- [191] Thomas T D 1984 *Phys. Rev. Lett.* **52** 417